The role of salt diapirism in controlling the sedimentology and distribution of deep-water deposits, Pierce Field, East Central Graben, North Sea.

Dr Clara Abu

Basins Research Group (BRG), Department of Earth Science & Engineering, Imperial College London

clara.abu07@imperial.ac.uk

Exhibition Rd, South Kensington, London SW7 2BX, United Kingdom,

Professor Christopher A-L. Jackson (he/him/his) | BSc, PhD, HonDUniv, CGeol, FGS, EurGeol

Director of Sustainable Geoscience | chris.jackson1@jacobs.com

5 First Street, Manchester, M15 4GU, UK

Malcolm Francis

Retired Geoscience Advisor | malcolm.francis1@gmail.com

Abstract

Passively rising diapirs control flank deformation (i.e., within 1 km of the salt-sediment interface) and resultant stratigraphic architecture of syn-kinematic units. Growth strata associated with deformation at the flanks of passive diapirs are known as halokinetic sequences. Very few studies

have conducted an integrated analysis of composite halokinetic sequences, CHS (stacked halokinetic sequences), and the damage occurring in host rocks during salt diapirism using seismic, petrophysical well data and core information.

This study integrates a 3D seismic reflection survey, core, and petrophysical data from the Pierce Field, northern North Sea, offshore UK to examine CHS in near-diapir strata and associated deformation. We recognize three tapered CHS in Units 6, 5, and 2. Two tabular CHS are recognized in Units 3 and 4, comprising the Miocene and Oligocene-aged sediments. The tapered CHS represents a rapid sediment-accumulation rate relative to the diapir-rise rate. The tabular CHS represents slow sediment accumulation rates relative to the diapir-rise rate.

Regarding near-diapir deformation, we observe large-scale fracturing associated with drape folding in the Ekofisk Formation resulting from the North and South Pierce salt movement. In the clastic successions, bedding parallel slip zones and slump folds dominate the Forties Sandstone Member and signify a destabilizing and rotational relationship of the Forties sandstone with the growing salt diapirs. Hybrid and remobilized flows interpreted from core data and lateral thickness changes support our interpretation of diapiric salt adjustment of deep-water deposition. Our study demonstrates the value of using an integrated dataset: 3D seismic reflection data and core to characterize the dynamic interaction between sediment gravity-flows and diapiric salt with North and South Pierce diapirs controlling thickness and facies distributions in the North Sea Central Graben.

Introduction

(Salt) diapirs are defined as a mass of salt that has flowed in a ductile manner and has discordant contacts with the enclosing overburden of rock or sediment (Jackson and Hudec 2017). Salt is a crystalline rock with an approximate density of 2,165 kg/m3. Near the surface, the density contrast between sediment and salt is very slight, however, the compaction of siliciclastic and carbonate rocks increases their density with depth resulting in the crystalline salt being less dense than the surrounding medium. Buried salt beneath denser overburden is buoyant and gravitationally unstable.

The diapiric rise of salt commonly drives and is associated with deformation (e.g., fracturing, folding, and potentially structural attenuation of near-diapir material) of the overburden rock or sediment (e.g., Barton 1933; Shultz-Ela et al. 1993; Jackson 1994; Evans et al. 1999; Giles 2002; Giles and Rowan 2012; Pichel and Jackson 2020; Rowan et al. 2020; Cumberpatch et al. 2021). Rowan et al. (2020) argue that wall-rock shearing during diapiric rise does not directly cause salt-induced deformation, but rather drape folding and associated fracturing of the diapirs roof. They also suggest that stratal thinning is largely depositional rather than structural. Alsop et al. (2000) demonstrate that the growth of salt diapirs in Nova Scotia, Canada resulted in the development of drag zones associated with significant attenuation and folding of the overburden, coupled with various styles of fracturing (see also Jackson and Talbot, 1991). Although initially attributed to wall rock shearing, deformation in this case could also now be reinterpreted to reflect roof-related deformation (Rowan et al. 2020). Similar styles of overburden deformation, including layer-parallel slip along lithologically distinct, mechanically weak layers, are observed adjacent to

diapirs in the northern North Sea, offshore UK and Norway, with this leading to the compartmentalization of carbonate and deep-water sandstone reservoirs trapped against the salt flanks (Davison et al. 2000).

The flanks of salt diapirs commonly have stratal upturns or steep beds, reflecting near-surface deformation of material next to the rising mass. These folds are of varying scales and origins. Deformation around diapirs can be at the minibasin-scale (i.e., several kilometres), with broad synclines forming within minibasins due to spatial changes in subsidence (i.e., near the thickest and densest part of the minibasin, which is typically near its centre) and uplift (i.e., of adjacent diapirs). A far narrower zone of drape folding (and thinning) of diapir roof strata occurs typically within 1 km of the salt-sediment interface (Giles and Rowan 2012). Growth strata associated with deformation at the flanks of passive diapirs are known as halokinetic sequences, a product of several episodes of burial, breakout, and downbuilding (Jackson and Hudec 2017). During downbuilding, the top of the diapir remains at or near the surface, with increased sedimentation of the overburden being matched by diapir rise (Barton, 1933). Halokinetic sequences are bound by angular unconformities that become correlative conformities away from the diapir, and which bound thinned and folded sediment wedges (Giles and Rowan 2012). Halokinetic sequences document the stratigraphic response to variations in the rate of near-surface diapir rise relative to local sediment accumulation, with two end-member types of halokinetic sequence. We recognize; hook halokinetic sequences, characterized by relatively tight (drape) folds and wedge halokinetic sequences, with reasonably open (drape) folds (Fig. 4a). Hook halokinetic sequences stack to form tabular composite sequences during slow sediment aggradation, when diapir rise rate outpaces sedimentation rate. These sequences are characterized by narrow (<200 m) zones of folding defined by abrupt facies changes towards the salt-sediment interface. For example, at El Papalote

Diapir, Mexico, Giles and Rowan (2012) report that mass-wasting deposits typically form the base of most hook sequences. These deposits result from the build-up of topographic relief, slow deposition of black-shale facies, and eventual failure of steep, unstable slopes. Wedge halokinetic sequences stack to form tapered composite sequences during relatively fast aggradation, when sediment accumulation rate outpaces diapir rise rate (Giles and Rowan 2012). Broad zones of folding (300-1000 m) characterize wedges, which internally are defined by relatively gradual facies changes. Hearon et al. (2014) use 3D seismic reflection and well data from the deep-water Auger Diapir, northern Gulf of Mexico to analyse composite halokinetic sequences in three dimensions, recognizing tapered and tabular sequences in Pliocene – Pleistocene turbidites flanking the salt body.

In addition to deforming adjacent rocks and sediment, salt diapirism can also control sedimentation patterns and the resultant stratigraphic architecture of syn-kinematic units. Mannie et al. (2016) illustrate how growth of salt structures formed from the flow of Lopingian salt of the Zechstein Supergroup had a dual control on the depositional thickness and facies distribution within a predominantly shallow-marine, Middle to Upper Jurassic synrift succession in the Norwegian Central North Sea. Hodgson et al. (1992) conclude that the presence of an extensive Permian salt basin underlying the Central Graben in the UKCS Northern North Sea strongly influenced patterns of tectonics and sedimentation in the area throughout the Mesozoic and Tertiary. Cumberpatch et al. (2021) investigate the exhumed Triassic (Keuper) Bakio and Guernica salt bodies in the Basque–Cantabrian Basin, Spain, concluding that the diapirs altered depositional systems, resulting in facies variability, remobilization of deposits, and channelization of flows, thus enabling better prediction of depositional architecture in areas where seismic imaging is challenging. In the North Sea, Zechstein Supergroup salt flowed to form large diapirs, including

those found in the North and South Pierce field areas. Halokinesis was marked by passive ascent of diapirs of Zechstein halite, which initiated in the Triassic and continued until the Miocene (Davison et al. 2000; Eldrett et al. 2015) with many diapirs occurring adjacent to, or directly above, large Mesozoic normal faults. These diapirs deformed the seafloor, resulting in intra-basin bathymetric highs, local slumping and the deflection of Paleogene sediment gravity flows (Davison 2005; Hempton et al. 2005). Subsequent salt movement deformed these deposits, induced steep dips, overturning and faulting stratigraphy, and generating clastic injections (e.g. Stewart 2006; Scott et al. 2010). In addition to salt-controlled bathymetric changes, relief associated with mass-transport deposits and fans of the earlier Maureen and Lista Formations (Danian–Selendian) also controlled the distribution of slightly younger, Sele Formation gravity flows (Paleocene). Later sediment progressively filled this relief, making the fan systems less confined (Johnson & Fisher 1998).

High-resolution three-dimensional seismic and outcrop datasets provide critical information on deformation and deposition adjacent to salt diapirs. For example, seismic data allow us to interpret large-scale geometry and reconstruct the evolution of salt-tectonic structures. Core and petrophysical data provide information on detailed, typically sub-seismic depositional and deformational processes. Very few studies have integrated datasets in this way. Here we review 3D seismic reflection, core, and petrophysical data from the Pierce Field, North Sea, offshore UK. We refine models of the tectonostratigraphic development of these two North Sea salt diapirs. In addition, we describe how to apply the concept of halokinetic sequences to this deep-water setting; We analyse the salt sediment interface and document uncertainties in reservoir pinch-out, onlap geometries, prediction of stratigraphic traps, and salt deformation patterns within the Upper Palaeocene, clastic-dominated, Forties Formation and the Lower Palaeocene, carbonate-

dominated, Ekofisk Formation; we investigate the dynamic interactions between sediment gravity flows in the Forties Sandstone Member and salt-induced relief. Our key aims are to identify, characterise, and deduce the controls on host rock deformation during salt diapirism.

Geological Setting

Our study area lies approximately 265 km east of Aberdeen between UK exploration blocks 23/22a and 23/27. This area is located above the Jæren High in the eastern margin of the UK Central Graben (Figs. 1 and 2). In a regional subsiding basin formed during the late Permian, evaporites dominate the Zechstein Supergroup deposits, particularly halite and locally clastic rocks. Thermal subsidence continued through the Triassic with halokinetic movement influencing the Triassic deposition, mostly red shales and siltstones. Finally, the Pangaea supercontinent started to break up, and during the Jurassic to early Cretaceous, thermal uplift and associated extension resulted in NW-trending, normal fault-bound horst and half grabens in the East Central Graben. Regional basin subsidence followed controlled by thermal cooling and loading of the continental crust during the Cretaceous and Cenozoic (Evans et al. 2003) (see Figs. 1 and 2).

Early Cretaceous strata comprise fine-grained clastic rocks, mainly claystones and sandstone-dominated deep-water mass-flow deposits and carbonates. In contrast, the late Cretaceous is dominated by chalk deposition and consists exclusively of remains of planktonic coccolithophorid algae and other pelagic organisms. Redeposited (allochthonous) chalk comprises slide, slump and debris-flow deposits, which form an important component of the Chalk Group in the Central Graben and alternates with autochthonous chalk (Perch-Nielsen et al. 1979; Watts et al. 1980).

Chalk debrites are abundant and well documented in many cores and well logs and make up much of the Tor Formation in the Ekofisk, Eldfisk, Valhall and Hod fields (Evans et al. 2003). During the Cretaceous, salt diapirs grew by periods of passive (i.e., syndepositional rise of a diapir as sediments accumulate around it) and active (i.e., buoyancy-driven rise beneath a relatively thin roof) diapirism. Chalk deposition was largely influenced by salt tectonics from Late Cretaceous times (Evans et al. 2003).

During the Paleocene (the focus of this study), the Scottish Highlands and the East Shetland Platform underwent a period of regional uplift associated with the development of the Iceland Plume, resulting in high sedimentation rates of siliciclastics into the basin (Evans et al. 2003). Additional stresses associated with the opening of the North-East Atlantic Ocean led to significant volcanic activity represented by the tuffs e.g. the late Paleocene Balmoral Tuffite unit in the Witch Ground Graben (Nadin and Kusznir 1995; Glennie 1998). The Paleocene interval is composed of several submarine fan systems (Den Hartog Jager et al. 1993; Jennette et al. 2000), within the Maureen and Lista formations, and lower part of the Sele Formation (Hempton et al. 2005; Davis et al. 2009). The deep-water sandstone-bearing part of the Sele Formation is assigned to the Forties turbidite fan system (Davis et al. 2009; Scott et al. 2010). During the Paleocene, active diapirism was particularly important during the latter stages of diapir growth. Carruthers et al. (2013) postulate that the overall wedge-shaped geometry of the Palaeocene stratigraphic interval suggests that North and South Pierce diapirs outpaced sediment supply linking this to a period of active diapiric rise.

The early Eocene Balder Formation caps the Forties Formation and is composed of claystone and volcanic tuffs. Middle Miocene sediments comprise fine-grained claystone and siltstones (Bowman, 1998). Polygonal faulting largely deforms the sequence from Eocene to the middle Miocene unconformity (MMU). Polygonal faults result from compaction and dewatering of mud-dominated sediment during early burial (Lonergan and Cartwright 1999; Cartwright et al. 2003). Diapiric salt growth was enhanced during the middle Miocene, driven by crustal shortening associated with the Alpine Orogeny (Oakman and Partington 1998; Davison et al. 2000a). Salt diapirism caused a local perturbation of the otherwise radially isotropic stress state, triggering local realignment of layer-bound fault patterns from polygonal to radial (i.e., fault strike normal to the salt-sediment interface) within middle Miocene claystone sequences next to the North and South Pierce salt stocks (Carruthers et al. 2013). A similar growth history is postulated for North and South Pierce salt stocks, exhibiting active growth (Paleocene & early Eocene) and passive growth (late Eocene, Oligocene, Pliocene & Pleistocene). The North Pierce diapir, however, is thought to have grown passively during the early Miocene, with minor pulses of active diapirism leading to the deposition of wedge-shaped halokinetic sequences. In this study, we focus on the Ekofisk Formation and the Forties turbidite fan member of the Sele Formation.

Dataset and methods

We use a 3D time-migrated seismic reflection dataset that covers an area of c. 2750 km^2. The data extends over UK blocks 23/22a and 23/27 (Fig. 1). The data were acquired initially by PGS and subsequently made public via DISKOS, the Norwegian government data archive (https://www.npd.no/en/diskos/). The data have an inline spacing of 25 m and crossline spacing of 25 m, with a sampling interval of 4 ms. Assuming an approximate frequency (31 Hz to 42 Hz) and

average interval velocity of 2822 ms-1 to 4916.13 ms-1. I estimate a vertical resolution of c. 23 - 29 m (wavelength $\lambda = V/f$, m; maximum vertical resolution = $\lambda/4$), and a horizontal resolution of c. 91 - 117 m for the interval of interest. These data are appropriate for detailed analysis of the geometry of the North and South Pierce salt stocks and the large-scale stratigraphic architecture and thickness of the Ekofisk Formation and the Forties Sandstone Member. The data are SEG reverse polarity, with a downward increase in acoustic impedance represented by a trough (red reflection) and a downward decrease by a peak (blue reflection). Water depths increase eastwards from c. -60ms to -130ms in the study area and several channel geometries are present in the near subsurface.

Boreholes are drilled within the study area and penetrate the stratigraphic intervals of interest. I perform detailed sedimentological core logging on six wells with a combined stratigraphic thickness of 341.94 m (23/22a-2, 23/22a-2z, 23/27-9, 23/27-5, 23/22a-3 & 23/27-7, see Fig. 6b for well locations). Data analysis involved lithology, grain size, bed thickness, type of bed contacts, and both primary and secondary sedimentary structures. Well-logs, including gamma ray, sonic, density and neutron, were available for petrophysical analysis, which I primarily used to infer lithology in un-cored well sections. 23/27-10 drilled through the Paleocene Forties Sandstone Member and reached total depth within the Paleocene Maureen Formation. 23/27-7, 23/27-5 and 23/22a-2z drilled through Paleocene Forties Sandstone Member and reached total depth within the Paleocene Ekofisk Formation. The 23/22a-3 drilled through the Paleocene Forties Sandstone Member and ended in the Upper Cretaceous Tor Formation. 23/27-9 and 23/22a-2 penetrate to deeper depths having drilled through the Paleocene Forties Sandstone Member, Ekofisk Formation and terminate in the Upper Permian Zechstein Group.

We use well-to-seismic tie (Fig. 3) process in Petrel software to relate horizon tops identified in a well with key seismic reflection events. The process involves using checkshot data from the seven exploration wells drilled in the study area to establish time depth relationship and to position the wells correctly in time. A synthetic seismogram is generated by convolving the reflectivity derived from acoustic and density logs with wavelet extracted from the seismic data. A fair-to-good well tie was established for well 23/27-7 and helped in calibrating the well tops to reflection events in seismic. We begin by mapping four main horizons across the dataset: Pleistocene, middle Miocene unconformity, Oligocene and Base Cretaceous unconformity. Locally we map the top Danian (Ekofisk Formation), top Forties Sandstone Member, and the early Eocene (Balder Formation). These surfaces form strong seismic markers which signify fundamental changes in sedimentation. We used the surfaces to calculate isopachs (i.e., stratigraphic thickness in ms TWT, Fig. 5) resulting in six main seismic stratigraphic units that show the distribution and evolution of sedimentary depocenters through time, as well as patterns and styles of diapir growth. We generate root mean square (RMS) seismic attribute for the Forties Sandstone Member to measure the internal reflectivity or energy from this unit. We utilize seismic-stratigraphic relationships and geometries to define and map unconformity-bounded packages (i.e CHSs) near the diapir flanks. The key indicator used to differentiate the different types of seismically imaged CHS are the geometry and the width of folding/stratal thinning. In addition we measure the width of the upturned zone for a horizon, defined as the section from the salt wall, which is vertical, to the point where the horizon returns to a regional level. We do not confidently map the geometry of the salt-sediment interface and diapir-flank stratal architecture due to the intensely faulted beds, steep dips, largely varying stratigraphic thicknesses and fair seismic resolution.

Results

Salt tectonic structural style

North and South Pierce salt stocks, sourced from Zechstein Supergroup evaporites, define the study area's salt-tectonic structural style. The salt stocks are slightly bulbous with weakly inclined stems. North Pierce is circular in map view and is c. 2.37 km long, c. 2.37 km wide, and c. 2.1 seconds tall on the two-way time seismic section. The South Pierce diapir is elongated and trends E-W, c. 4.1 km long, c. 3.2 km wide and 3.1 seconds tall on the two-way time seismic section. The width of diapirs is hard to define, given that the salt sediment interface is only well-imaged on the upper part of the stocks; hence, we define this where there is a breakdown in the continuity of overburden sediment reflections. Both salt stocks penetrated the Chalk and much of the overlying Tertiary sediments. For example, South Pierce cuts up into Pliocene sediments, whereas North Pierce extends up to below the mid-Miocene unconformity. There is evidence of erosion and complex faulting over the structure (Fig. 6). The complex radial faulting represents contractional active diapirism between the Pleistocene and the present, with faults trending NW parallel to the structural trend between both salt stocks.

Near diapir stratigraphic architecture

We focus our analysis on the composite halokinetic sequences (CHS) geometries of near-diapir strata preserved adjacent to the North and South Pierce diapirs. We use the seismic to define the large-scale architecture, and the well-logs, including gamma ray, sonic, density, and neutron, for petrophysical analysis. We start with the oldest and deepest, unit 6, progressing upwards to the

seabed (see Fig. 6b for locations of borehole correlations, arbitrary composite lines, inline, and crosslines illustrating the units, Figs. 6a, 7, 8-11).

Unit 6 (Ekofisk Formation)

Unit 6 is stratigraphically equivalent to the Ekofisk Formation and is bound above and below by the top Danian and Base Cretaceous unconformity reflection, respectively. Unit 6 thins slightly to the north but overall thickens basinward (i.e., towards the SSE, Figs 5a, 6-7, 8-11). Seismic stratigraphic analysis of unit 6 shows a regional broad and gentle drape-fold geometry. Toward the stocks, Unit 6 exhibits gently convergent bounding surfaces; hence I classify it as a tapered CHS (Fig. 4a). Folding and thinning occur over a horizontal width of c. 935 m, with only minor and gradual bed rotation (Fig.6). Bounding unconformities define high-angle truncations ($<60^{\theta}$) of underlying reflections. Only one of the drilled wells, 23/27-9 (Fig. 7), penetrated the Base Cretaceous; therefore, we cannot evaluate the regional changes in lithology associated with the observed seismic stratigraphic architecture.

Unit 5 (Sele, Lista, and Maureen Formations)

Unit 5 is stratigraphically equivalent to the Sele, Lista, and Maureen Formations and is bound above and below by the early Eocene and top Danian reflection, respectively. Regional thickness changes within the survey area (see Fig. 5b) for Unit 5 vary from c. 80 ms to 240 ms. Overall, Unit 5 thickens basinward (i.e., NW-SE; Figs 5b, 6a, 7, 8-11). The isochore map shows a local thickening wedge that deflects around North Pierce and ponds behind the South Pierce diapir. Superimposed on these regional changes are local, near-diapir thickness changes. Near-diapir strata show the upper and lower bounding surfaces of Unit 5 gently converge towards the diapir; hence I classify it as a tapered CHS (Fig. 4a). Folding and thinning occur over widths c. 930 m,

with only minor and gradual bed rotation (Figs. 5a, 7, 8 and 10). Bounding unconformities have high angle truncations ($<55^{\theta}$) of underlying reflections.

The wells 23/27-9 (NE), 23/27-5 (E), and 23/27-10 (SW) are drilled near the South Pierce diapir, while well 23/27-7 is drilled further basinward, to the far south of South Pierce. Wells 23/22a-2 (SW), 23/22a-2z (SW), and 23/22a-3 (E) are close to North Pierce. The well-log correlation panels (Figs. 7, 9a, and 11) show that unit 5 thins towards the South and North Pierce salt stocks, an observation consistent with the seismic data. There is a considerable thickening of this unit c. 362 m to the south in the 23/27-7 well. One of the units of interest, the Forties Sandstone Member, is present within Unit 5. Sandstone thickness changes considerably from well to well. The Forties Sandstone Member shows a high degree of correlation between wells 23/27-10 and 23/27-7 but bears little resemblance in well 23/27-9 (see Fig. 7). The proximity of 23/27-9 well to the South Pierce salt stock seems to be a key factor. There is a good correlation of the Forties Sandstone Member in wells 23/22a-3 and 23/27-5 (Fig. 9a), but both wells show no obvious correlation to 23/27-9. Similarly, the Forties Sandstone Member shows a high degree of correlation between wells 23/22a-2z and 23/22a-3 but bears little resemblance in well 23/22a-2 (see Fig.11). The proximity of 23/22a-2 well to the North Pierce salt stock seems to be a key factor. The time structure map of the top Forties Sandstone Member shows overall basin geometry with the basin deepening towards the SSW. The RMS amplitude map shows high reflectivity and laterally extensive reflection packages that trend NW-SE.

Unit 4 (Horda and Balder Formations)

Unit 4 is stratigraphically equivalent to the Horda and Balder Formations and is bound above and below by the top Oligocene and early Eocene reflection, respectively. Regional thickness changes (see Fig.5c) within the survey area for Unit 4 vary from c. 600 ms to 1100 ms. Overall, Unit 4 thickens to the north and west. Superimposed on these regional changes are local, near-diapir thickness changes. Near-diapir seismic stratigraphic analysis of Unit 4 shows narrow and steep drape-fold geometry. This unit comprises hooks (Figs. 6a, 8 and 10) that stack vertically to form tabular composite halokinetic sequences (CHS), with parallel to sub-parallel, upper and lower bounding surfaces. Folding and thinning of the sediment range from 150 m – 190 m in width and display taper angles c.>70^{θ}.

Unit 3 (lower Lark Formation)

Unit 3 is stratigraphically equivalent to the lower Lark Formation and is bound above and below by the Mid Miocene unconformity and the top Oligocene, respectively. Unit 3 thickens basinward (i.e., towards the south; Figs 6a, 8 and 10). This unit's regional thickness changes (Fig. 5d) vary from c. 300 ms near the salt-sediment interface to 750 ms basinward. Near-diapir analysis shows tabular composite halokinetic sequences (CHS), with parallel to sub-parallel, upper and lower bounding surfaces (see Figs. 6a, 8 and 10). Folding and thinning ranges from 120 m – 170 m in width and display taper angles c.>70°.

Unit 2 (upper Lark Formation)

Unit 2 is stratigraphically equivalent to the upper Lark Formation and is bound above and below by the top Pleistocene and the Mid Miocene unconformity, respectively. Seismic stratigraphic

analysis of unit 2 (Figs 5e, 6a, 8 and 10) shows a large-scale wedge geometry dipping to the SE. The unit's upper and lower bounding surfaces gently converge towards the diapir; hence I classify it as a tapered CHS. Folding and thinning ranges from 120 m – 170 m in width and display taper angles c.>70^{θ}. The Mid Miocene unconformity onlaps the South Pierce salt diapir, and sediments truncate and onlap against it.

Unit 1 (Nordland Group)

Unit 1 is stratigraphically equivalent to the Nordland Group and is bound above and below by the seabed and top Pleistocene. The thickness gradually increases to the northwest from c. 250 ms to c. 700 ms (Figs. 6a, 8 and 10). The Nordland Group marine claystone deposited during subsidence of the Central Trough dominates this unit. The North and South Pierce diapirs do not penetrate this stratum.

Sedimentary facies

Based on the description of selected intervals of core data from seven wells, I identify eight main facies used to characterise the Forties Sandstone Member and the Ekofisk Formation: (i) thick-bedded sandstones; (ii) thin-bedded sandstones; (iii) banded sandstones; (iv) hybrid beds; (v) slurry flows (vi) debrites; (vii) mudstones and (viii) chalk (see Table 2 for detailed description).

Syn-depositional and post-depositional features

Near-salt deformation during passive salt rise is related mainly to the drape folding of a thin roof, which results in associated fracturing. Seismic imaging adjacent to and below the diapirs is poor,

making it difficult to interpret structural features such as faults. Core data therefore provide valuable information on sub-seismic, small-scale deformational features located close to the salt diapirs. In this section, I summarize structures (both sedimentary and non-sedimentary) that record syn-depositional and post-depositional deformation.

Syn-depositional deformation: Most passive diapirs are accompanied by syn-depositional drape folds defined by strata upturn that is typically restricted to within 1 km of the salt-sediment interface (halokinetic sequences). Halokinetic sequences commonly exhibit or contain local breccias or reworked sediments that thin and ultimately pinch-out away from diapiric salt. The reworked sediments (debrites) are typically located just above unconformities located within and that define individual packages within halokinetic sequences. They typically form when significant weak, typically very fine-grained sediments are deposited on or immediately adjacent to the diapir, leading to bedding-parallel flexural slip and sliding as the sedimentary layer thins over the diapir. Well, 23/27-9 shows examples of such soft-sediment deformation within reworked sediments.

Post-depositional deformation: Small-scale fractures are rare. However, opening-mode fractures and veins are common in wells 23/22a-2 and 23/22a-2z. 23/22a-2 notably contains bedding-parallel conjugate fracture sets. These fractures might record minor bed-parallel lengthening or extension due to outer-arc extension during halokinetic folding. The first set may have formed when roof strata were initially folded over the growing diapir, whereas the second, conjugate set may have formed later, when strata had been rotated to dip sub-vertically or at least relatively steeply (Rowan et al., 2020).

Discussion

The following three sections discuss the style and controls on: (a) damage occurring in host rocks during salt diapirism, (b) seismic-scale composite halokinetic sequences and (c) control of salt diapirs on deep-water sedimentation.

Damage occurring in host rocks during salt diapirism.

Folding, fracturing, and shearing of strata are common processes on the flanks of diapiric salt (Wallace, 1944, Jackson and Talbot, 1991; Alsop et al., 2000). Folds associated with diapiric salt rise have been attributed to drag/shear of adjacent strata or syndepositional drape folding (Jackson et al., 1990; Alsop et al., 2000; Davison et al., 2000a; Stewart, 2006). Radial extensional faults are observed over the crests of buried, active diapirs (due to doming) and on diapir flanks. Radial faults on diapir flanks may have formed in roof strata and subsequently rotated into diapir-flanking positions by drape folding (Rowan et al., 2020) or formed by hoop stress and stem push (Jackson and Hudec, 2017; Coleman et al., 2018). Small-scale deformation, such as low-displacement faults and shear zones, are reported from outcrop examples and wells (Alsop et al., 2019; Alsop et al., 2016, 2018; Davison and Barreto, 2020). More recently, Rowan et al. (2020) concluded that diapir rise and emplacement do not directly shear and fracture adjacent strata, using examples from exposed salt structures, such as in Paradox Basin of the southwest USA, La Popa Basin in northeastern Mexico, the Prebetics of SE Spain and the Flinders and Willouran Ranges of South Australia. They instead propose that salt movement leads to drape folding and predominantly depositional (rather than structural) thinning of the roof, which may cause associated fracturing.

This study shows that the North and South Pierce diapirs grew from the Triassic through to the Miocene, an interpretation consistent with that proposed by Davison et al. (2000). However, their growth was complex and included three growth modes:

1. Passive diapirism occurred when the salt was at or very near the seabed, and the diapir was supplied with salt expelled from beneath adjacent, downbuilding minibasins (Triassic to Eocene).
2. Periodic diapir burial (i.e., during the early Miocene) when sediments aggraded faster than the diapir crest rose.
3. Active diapirism occurred when the diapir was buried, with diapiric rise driven by shortening (Paleocene and middle Miocene).

We see evidence for near-diapir deformation in both carbonate and clastic successions. For example, in the North and South Pierce stocks, active piercement and buoyancy forces create periodic episodes of topographic relief at the diapir crests, resulting in the Ekofisk Formation chalk slumping and sliding off the crests of the diapirs. Although we see no evidence for soft-sediment slumping in the cored examples from the Chalk, Davison et al. (2000) report this, halite and anhydrite debrite, and bedding-parallel fault zones in chalk from the Kyle Field, Central North Sea, using the presence of these features to argue that the salt was exposed and very near the seabed during the Late Cretaceous to Palaeocene, and that the associated topographic relief was several tens to hundreds of meters.

We see core-scale evidence for large-scale fracturing, pressure solution, and significant extensional faulting, which together combine to thin the overburden along the flanks of the South

and North Pierce stocks as they rise. For example, we observe numerous interconnected calcite-filled fractures in the Ekofisk Formation, North Pierce Field (Figs. 18a, b and c) and postulated to have formed from pressure solution (Simon-Robertson, 1992). Fluid transfer in chalk cores is also present from the Machar and Banff fields (Davison et al., 2000). Intensely fractured intervals, with several intersecting fracture sets, are also present in the Chalk. These point to several phases of fracture opening, with wall-rock slivers separating 'crack and heal' events (Simon-Robertson, 1992). We observe multiple thread-like fractures at high-angle to bedding, filled by calcite. The most significant number of high-angle open fractures are observed in the Tor Formation from the 23/27-9 well (i.e., located c. 400 m from the South Pierce stock) and within the Tor and Mackerel Formation in the deeper cores recovered in the 23/22a-2 well (i.e., located only c. 100 m from the North Pierce stock). These fractures indicate that rising salt stretched and thinned the Ekofisk Formation overburden. Bedding-parallel micro-stylolite swarms are common and may indicate small-scale pressure solution at specific bedding surfaces.

High-angle discordant Neptunian sandstone dyke injections (Fig. 19b.) within the Ekofisk Formation suggest a largely fractured Ekofisk Formation. Simon-Robertson (1992) suggest that the fractures within the Ekofisk Formation were open during the early stages of Maureen Formation deposition, with these sandstones subsequently injected into the fractures. The sands within the dyke system have a similar grain size to the overlying Maureen Formation. Past studies have shown evidence for sand injection in the overlying Maureen Formation due to dewatering and soft sediment deformation. It is common for such fabric to extend into an underlying Ekofisk Formation (Simon-Robertson 1992). These fractures were not formed as a direct response to salt movement. We propose these fractures occurred following near-seabed lithification of the chalk

(due to mechanical and chemical compaction of the Ekofisk Formation) and drape folding as the salt maintained some topographic relief. We observe stylolites and microstylolite swarms from core data, evidence for pressure solution, and chemical compaction. These fractures created some porosity in the Ekofisk Formation, although now cemented by calcite based on observations in the core data. Although rare in our study, there are examples of chalk debrite in cores from other wells in the Central North Sea (Davison et al. 2004).

In terms of halokinesis-related deformation in clastic-dominated successions, our study of the South and North Pierce diapir flanks shows substantial seismic-scale thinning of strata towards the diapir flanks, including within the Forties Sandstone Member. Unit 6 and other units also increase in dip with increasing proximity to the salt-sediment interface. In core data, however, we see limited evidence for the fracturing and minor faulting in the Forties sandstones. However, slump folds and bedding parallel slip surfaces from the core data in mudstone within the Forties Sandstone Member (Fig. 16d). Some authors have reported extensional slide zone in wells drilled close to salt diapir margins and slump folds due to lateral compression and internal shearing (Davison et al., 2000; Cumberpatch et al., 2021). Bedding-parallel flexural slip/flow during halokinetic drape folding results in shear zones (Rowan et al., 2003; 2016; Rowan and Ratliff, 2012). We infer that this style of near-diapir deformation occurs in response to a diapir near the surface, probably during the Paleocene to Miocene period. We envisage high sediment accumulation rates will cause positive relief on the salt diapir crest. Faulting and rotation of the sediments lead to slumping due to the topographic relief.

Seismic-scale composite halokinetic sequences

Near-surface deformation of sediment next to rising salt diapirs occur in many deep-water environments, such as the Central Graben, North Sea; Gulf of Mexico and the Central Flinders Ranges, South Australia (e.g., Hodgson et al. 1992; Vendeville & Jackson, 1992; Davison et al., 2000; Giles & Lawton, 2002; Schultz-Ela, 2003; Rowan et al., 2003; Giles & Rowan, 2003; Kane et al. 2012; Andrie et al., 2012; Kernen et al., 2012; Giles & Rowan, 2012; Hearon et al., 2014). Near-diapir sediment deformation and associated changes in stratal thickness occur at two scales: (1) minibasin-scale, due to the development of broad, synclinal folds that span the entire width of a minibasin; and (2) diapir-flank scale, related to a narrow zone of drape folding and thinning of diapir roof strata during diapir rise. Syn-kinematic, unconformity-bound packages adjacent to diapir-flanks are known as halokinetic sequences, which stack to form composite halokinetic sequences. Outcrop and the subsurface data provide several examples of halokinetic sequences (e.g., Giles and Lawton, 2002; Rowan et al., 2003; Giles and Rowan, 2012; Andrie et al., 2012; Kernen et al., 2012; Carruthers et al., 2013; Hearon et al., 2014, 2015a, 2015b; Harrison and Jackson, 2014; Saura et al., 2014, 2016; Poprawski et al., 2014, 2016; Rojo et al., 2016; Martín-Martín et al., 2016; Rojo and Escalona, 2018; Coleman et al., 2018; Pichat et al., 2019; Snidero et al., 2019; Davison and Barreto, 2020; Verg´es et al., 2020; Pichel and Jackson, 2020; Gannaway-Dalton et al., 2020a). The deformation and associated impact on the deposition of CHS is related to the height and extent of local topographic relief over passive diapirs, which are a result of the interplay between sediment-accumulation rate and diapir-rise rate (Giles et al., 2012). Sediment accumulation rates are a function of lithology and depositional environment. Tabular CHS typically develop during or after prolonged periods of slow deposition with the formation of significant topographic relief over the diapir, resulting in thin roofs, narrow zones of drape folding,

scarp failure, erosion, and possible common mass wasting. Folding and thinning occur over a narrow zone within 200 m of the diapir surface. Tapered CHS typically form when the sediment accumulation rate adjacent to the diapir exceeds the diapir-rise rate over the timescale of a third-order depositional sequence. Thinning and upturn typically occur over a horizontal distance of c. 1 km.

The North Sea Basin offers an excellent opportunity to examine the controls on composite halokinetic sequence (CHS) development. I see seismic-scale evidence for tapered composite halokinetic sequences from strata flanking the North and South Pierce stocks, with the upper and lower bounding surfaces of Units 5 and 6 gently converging, over a horizontal distance of c. 1 km, towards the salt-sediment interface. This geometry is indicative of a period when sediment-accumulation rate outpaced the diapir-rise rate, resulting in the build-up of a relatively thick diapir roof and formation of a relatively wide zone of drape folding. The Forties Sandstone Member sits within Unit 5, a tapered CHS, with the deep-water submarine fan system it defines likely characterised by relatively high (compared to hemipelagic and pelagic processes) sediment accumulation rates. Several authors have demonstrated examples of tapered CHS (e.g., Davison et al. 2000; Giles et al. 2012; Johnson & Bredeson 1971; Rowan et al. 2003), using several subsurface examples from deep-marine settings. Giles et al. (2012) report tapered CHS in Plio-Pleistocene strata in the Northern Gulf of Mexico, with stratigraphic thinning and upturn occurring over 0.5-1 km. In the Central North Sea, Davison et al. (2000) report thinning and upturn near the South Pierce diapir with local angular unconformities at the Top Paleocene reservoir level, consistent with our observations.

We observe several onlap surfaces in Units 3 and 4 (see Figs. 6a, 8 and 10), which suggests diapirs were actively rising during this period and indicating that topographic relief partially controlled sediment pathways. This observation agrees with Davison et al. (2000), who suggest significant unconformities developed locally above the diapirs during the Palaeocene and middle Miocene. Reactivation and active rise of diapirs represents periods when the relative upward movement of the diapir was greater than sediment accumulation rates. The rapid growth led to significant sea-bed relief, with high-angle onlap above the related unconformities. This observation is consistent with the tabular CHS we observe below the Mid-Miocene unconformity.

We observe a gentle convergence of the upper and lower bounding surfaces of units 1 and 2 towards the North and South Pierce diapirs. This seismic stratigraphic relationship suggests a tapered CHS, which dominated the Pliocene – Pleistocene period suggesting that sedimentation rates outpaced the salt rise rate, burying the salt.

Control of salt diapirs on deep-water sedimentation

Salt-related topography influences submarine sedimentary systems in many deep-water environments, such as the Gulf of Mexico, offshore West Africa, the eastern Mediterranean, and northern Spain (e.g., Posamentier & Kolla, 2003; Gee & Gawthorpe, 2006; Clark & Cartwright, 2009; Mayall et al., 2010; Kane et al., 2012; Oluboyo et al., 2014; Doughty-Jones et al., 2017; Rodriguez et al., 2019; Cumberpatch et al., 2021). Salt-cored folds pond, divert, deflect, block, or confine turbidite systems (Prather et al., 1998; Kneller, 2003; Prather, 2003; Smith, 2004; Clark & Cartwright, 2009). In the Magnolia Field, Gulf of Mexico allochthonous salt controlled the development of Pleistocene submarine channel systems, which were initially deeply entrenched

close to the salt, but that progressively avulsed down the lateral slope in response to ongoing diapir rise (Kane et al. 2012). The exhumed Triassic (Keuper) Bakio Diapir in the Basque–Cantabrian Basin, northern Spain is flanked by deep-water carbonate (Aptian–earliest Albian Urgonian Group) and siliciclastic (middle Albian– Cenomanian Black Flysch Group) successions. These successions exhibit unconformity-bounded sedimentary wedges that thin towards and upturn against the diapir. Cumberpatch et al. (2021) report that the failure of carbonate platforms developed above the crests of the active Bakio diapir emplaced debrites in the adjacent minibasin, proximal to the salt-sediment interface, and generated local topography that also constrained clastic-dominated, axial depositional systems. Indicators of syn-depositional dynamic topography, such as debrites, hybrid beds, remobilized strata, and lateral thickness changes over short distances collectively support an interpretation of halokinetic modulation of a deep-water deposition.

The interaction between salt-induced seabed relief in the Central North Sea controlled Paleocene turbidite sandstone deposition and distribution. For example, the Forties fan system built out broadly south-eastwards into the North Sea Central Graben, being predominantly deposited around and having its thickness and facies distributions controlled by active salt diapirs, such as North and South Pierce (Davison et al., 2000; Davison, 2004 and Eldrett et al., 2015). Davison et al. (2000) report that Chalk thins from c. 1500 m on the flanks to 0-300 m above the diapir. Our isochore map of Unit 5 (Fig. 5b), which contains the Forties Sandstone Member, shows substantial regional thickening basinward from the North and South Pierce diapirs, i.e., from c. 80 ms to 240 ms. A thickening wedge deflects around North Pierce and ponds behind the South Pierce diapir (Fig. 5b), comparable to findings by Davison et al. (2000), who suggest that the thickening reflects sediments (sand-prone complex) sliding off the salt stock's crest. This wedge indicates topographic

relief on the diapirs' controlled sediment transport pathways by deflecting sediments from its crest towards the flanks. The well-log correlation panel also supports a substantial thickening of the Forties Sandstone Member basinward (Fig. 7). Based on core data analysis from wells drilled close to the flanks of the diapirs, I observe soft-sediment deformation and sandstone dyke injection in the Forties Sandstone (Figs. 19b). This is consistent with Cumberpatch et al's. (2021) observation that hybrid and remobilized beds may point toward destabilization and slumping of the Forties sandstone above the growing salt diapirs. In addition, thickness changes support the interpretation of a Paleocene (Forties fan) system deflected by the topography and structural features created by the actively growing salt diapirs.

Lateral variations in core facies proportions in the Forties Sandstone Member in 23/22a-3, 23/27-9 and 23/27-5

Description – In 23/27-5, the Forties Sandstone Member begins with a thinning-upward, very-fine-grained to fine-grained sandstone sequence containing numerous interbeds of green, waxy, angular to sub-rounded, clast-rich claystones and minor siltstone. A thickening-upward unit comprising mainly thick-bedded sandstones immediately overlies the underlying unit and in contrast, is clast-free. This zone is, however, rich in dewatering and water-escape pipes, predominantly in the lower part of the sandstone, with dish structures becoming more common in the upper sections. Mud-rich and sand-rich bands predominate in the uppermost sections. A thinning upward sequence, capped by a hemipelagic blanket, caps this interval. Facies F1 (thick-bedded sandstones), F2 (thin-bedded sandstones), F4 (hybrid beds) and F5 (slurry beds) dominate the cored interval of the Forties Sandstone Member.

The Forties Sandstone Member is thin in 23/27-9 (400 m away from the South Pierce diapir), with F2 (thin-bedded sandstones) and F5 (slurry beds) dominating the interval. Stratigraphic organisation is not obvious in this well. A thick unit of claystone overlies the sandstone. In 23/22a-3, F1 (thick-bedded sandstones), F2 (thin-bedded sandstones), and F5 (slurry beds) dominate the cored interval.

Three distinct facies are recognized in the Forties Sandstone Member based on examining cores obtained in 23/22a-3, which lies east of the North Pierce diapir, and 23/27-9 and 23/27-5 which lie to the NE and E, respectively, of the South Pierce diapir (see Figs. 9a and 9b). The internal facies architecture of the Forties Sandstone Member is complex. The pie chart shows a common occurrence of thick-bedded, debrite, slurry flows, and mudstone facies in all three wells. An observation of the facies distribution in each well in the pie-chart highlights the lateral change in facies character of the gravity flow deposits within a distance (1km-400 m – 0.8 km) taken along the strike section of the Forties Sandstone Member fairway. The distribution and thickness of the sandstone change considerably from well to well with high facies variability predominantly in the 23/27-9 well, 400 m adjacent to the diapir. The high facies variability between the 23/22a-3 and 23/27-5 wells to the 23/27-9 well makes the correlation between these three wells subjective (Fig. 20). The sandstone packages in wells 23/22a3 and 23/27-5 wells are well-developed and highly correlatable but bear little resemblance to the 23/27-9 well.

Interpretation – the facies variability between the three wells (23/22a-3, 23/27-5 and 23/27-9) suggests the proximity of 23/27-9 well to the South Pierce salt stock is a key factor. The sands in

the 2322a3 well comprise massive thick beds with injections and mud clasts, but within approx 0.8 km in the 23279 well, there is a local increase in the thickness and distribution of reworked sediments and sheared fabric, close to the South Pierce diapir. In summary, 23/22a3 and 23/27-5, which are on the north-eastern side of the South Pierce diapir, can be correlated reasonably well, showing that thick-bedded and banded sandstones, debrites, and slurry flows are laterally rather extensive. However, the facies identified in these wells differ to those in 23/27-9, which is-located 100 m, adjacent to the diapir; here, hemipelagic mudstone (F7) is more common, suggestive of deposition outside of a channel or lobe. In 23/27-9, the Forties Sandstone Member comprises coarsening-upwards packages and that are capped by a unit containing thin interbeds of dark-grey mudstone. High-concentration turbidity currents (F1) are the primary transport mechanism for the Forties Sandstone Member. The thickly bedded units result from rapid, en mass deposition from sand-rich flows (Baas, 2011; Mulder & Alexander, 2001; Mutti & Ricci Lucchi, 1978; Stow & Johansson, 2000; Talling 2012). The numerous green claystone clasts in 23/27-5 may be rip-up clasts derived from the underlying Maureen Formation.

The presence/absence and distribution of MTCs in the context above

In light of the correlation above, the core facies in the Forties Sandstone Member in 23/27-9, which is closest to the diapir, reveals an increased presence of debrite-related material and sheared fabric attributed to remobilization of sediments due to diapir growth and related seabed deformation.

Conclusions

Our interpretation of this legacy 3D time migrated seismic reflection data combined with existing core data enabled us to use the Pierce field as a natural laboratory to improve our understanding

of salt diapirism and its control on sedimentology and distribution of deep-water deposits. This study further illustrates the value of making legacy data available for training and academic study.

(1) Evidence for near-diapir deformation in both carbonate and clastic successions, such as, large-scale fracturing, pressure solution, and significant extensional faulting along the flanks of South and North Pierce stocks, in the Ekofisk Formation are associated with drape folding resulting from salt movement. A predominance of multiple sets of fractures and calcite-cemented fractures in the Ekofisk Formation signify bending related stretching due to diapiric salt rise. Bedding parallel slip zones and slump folds are dominant in the Forties Sandstone Member and signify a destabilizing and rotational relationship of the Forties sandstone with the growing salt diapirs.

(2) We identify three tapered composite halokinetic sequences in Units 6, 5, 2 and two tabular composite halokinetic sequences in Units 3 & 4 (Miocene and Oligocene aged sediments). The tapered CHS represent rapid sediment-accumulation rate relative to diapir-rise rate. The tabular CHS represents slow sediment accumulation rates relative to diapir-rise rate.

(3) The Forties fan system regionally thickens basinwards (broadly south-eastwards) into the North Sea Central Graben, being predominantly deposited around and having its thickness and facies distributions controlled by the North and South Pierce diapirs. Hybrid and remobilized flows interpreted from core data and lateral thickness changes supports our interpretation of diapiric salt modification of deep-water deposition.

(4) An integration of core data, petrophysical logs and seismic provides a better understanding of salt-sediment interaction especially in basins where seismic imaging is challenging.

References

Ahmadi, Z. M., Sawyers, M., Kenyon-Roberts, S., Stanworth, C. W., Kugler, K. A., Kristensen, J. and Fugelli, E. M. G. 2003. Paleocene. In: Evans, D., Graham, C., Armour, A. & Bathurst, P. (eds) The Millennium Atlas: Petroleum Geology of the Central and Northern North Sea. Geological Society, London, 235–259.

Alsop, G.I., 1996. Physical modelling of fold and fracture geometries associated with salt diapirism. In: Alsop, G.I., Blundell, D.J., Davison, I. (Eds.), Salt Tectonics, 100. Geol. Soc. Spec. Pub., pp. 227–241. https://doi.org/10.1144/GSL.SP.1996.100.01.14

Alsop, G.I., Brown, J.P., Davison, I., Gibling, M.R., 2000. The geometry of drag zones adjacent to salt diapirs. J. Geol. Soc., London 157, 1019–1029. https://doi.org/ 10.1144/jgs.157.5.1019.

Alsop, G.I., Jenkins, G., Davison, I., 1995. A preliminary study of drag zone geometry adjacent to salt diapirs. In: Travis, C.J., Harrison, H., Hudec, M.R., Vendeville, B.C., Peel, F.J., Perkins, B.F. (Eds.), Salt, Sediment, and Hydrocarbons. 16th Annual GCSSEPM Foundation Bob F. Perkins Res. Conf., pp. 1–9. https://doi.org/10.5724/ gcs.95.16.0001

Alsop, G.I., Weinberger, R., Levi, T., Marco, S., 2016. Cycles of passive versus active diapirism recorded along an exposed salt wall. J. Struct. Geol. 84, 47–67. https:// doi.org/10.1016/j.jsg.2016.01.008.

Alsop, G.I., Weinberger, R., Marco, S., Levi, T., 2018. Fault and fracture patterns around a strike-slip influenced salt wall. J. Struct. Geol. 106, 103–124. https://doi.org/ 10.1016/j.jsg.2017.10.010.

Alsop, G.I., Weinberger, R., Marco, S., Levi, T., 2019. Identifying soft-sediment deformation in rocks. J. Struct. Geol. 125, 248–255. https://doi.org/10.1016/j. jsg.2017.09.001.

Andrie, J.R., Giles, K.A., Lawton, T.F. and Rowan, M.G. 2012. Halokinetic-sequence stratigraphy, fluvial sedimentology and structural geometry of the Eocene Carroza Formation along La Popa salt weld, La Popa Basin, Mexico. Geological Society special publication. 363 (1), 59–79. doi:10.1144/SP363.4.

Baas, J.H., Best, J.L. and Peakall, J. 2011. Depositional processes, bedform development and hybrid bed formation in rapidly decelerated cohesive (mud–sand) sediment flows. Sedimentology, 58, 1953-1987.

Barker, S.P., Haughton, P.D., McCaffrey, W.D., Archer, S.G. and Hakes, B. 2008. Development of rheological heterogeneity in clay-rich high-density turbidity currents: Aptian Britannia Sandstone Member, UK continental shelf. Journal of Sedimentary Research, 78, 45-68.

Barton, D. C. 1933. Mechanics of formation of salt domes with special reference to Gulf Coast salt domes of Texas and Louisiana. American Association of Petroleum Geologists Bulletin, 17, 1025–1083.

Bouma, A. H. 1962. Sedimentology of some flysch deposits: A graphic approach to facies interpretation: Amsterdam, Elsevier, 168 p

Bowman M.B.J in Glennie, K.W. 1998 Petroleum geology of the North Sea : basic concepts and recent advances. Fourth edition. Oxford, Blackwell Science.

Carruthers, D., Cartwright, J., Jackson, M.P.A and Schutjens, P. 2013. Origin and timing of layer-bound radial faulting around North Sea salt stocks: New insights into the evolving stress state around rising diapirs. Marine and petroleum geology 48: 130-148.

Cartwright, J., James, D., Bolton, A. 2003. The genesis of polygonal fault systems: a review. In: Van Rensbergen, P., Hillis, R.R., Maltman, A.J., Morley, C.K. (Eds.), Polygonal Faults and Sediment Mobilization, Geological Society, London, Special Publications, vol. 216, pp. 223-243.

Charles, R., and K. Ryzhikov. 2015 “Merganser Field: Managing Subsurface Uncertainty During the Development of a Salt Diapir Field in the UK Central North Sea.” Geological Society special publication 403.1 1–3. Web.

Clark, I.R. & Cartwright, J. 2009. Interactions between sub-marine channel systems and deformation in deepwater foldbelts: examples from the Levant Basin, Eastern Mediterra-nean sea.Mar. Petrol. Geol.,26, 1465–1482

Coleman, A.J., Jackson, C.A.-L., Duffy, O.B., Nikolinakou, M.A., 2018. How, where, and when to radial faults grow near salt diapirs? Geol. 46, 655–658. https://doi.org/ 10.1130/G40338.1.

Collinson, J. and Mountney, N. 2019. Sedimentary structures. Edinburgh, Dunedin Academic Press.

Cumberpatch, ZA., Kane, I.A., Soutter, E.L., Hodgson, D.M., Jackson, C.A.-L., Kilhams, B.A., Poprawski, Y. 2021. Interactions between deep-water gravity flows and active salt tectonics SEPM; 2021 DOI: 10.2110/jsr.2020.047

Davison, I., Barreto, P., 2020. Deformation and sedimentation processes, and hydrocarbon accumulations on upturned salt diapir flanks in the Lusitanian Basin. Portugal. Pet. Geosci. https://doi.org/10.1144/petgeo2019-138.

Davison, I., Alsop, G.I., Evans, N.G and Safaricz, M. 2000a. Overburden deformation patterns and mechanisms of salt diapir penetration in the Central Graben, North Sea. Marine and petroleum geology 17(5): 601-618.

Davison, I., Alsop, G.I., Birch, P., Elders, C., Evans, N, Nicholson, H., Rorison, P., Wade, D., Woodward, J. and Young, M. 2000b. Geometry and late-stage structural evolution of Central Graben salt diapirs, North Sea. Marine and Petroleum Geology 17 (2000) 499-522

Davison, I. 2004. Bathymetric controls on Paleocene gravity flows around salt domes in the Central Graben, North Sea. GCSSEPM 24 Th Annual Meeting, Bob Perkins Research Conference, December 5 Th -8 Th 2004 , Houston Texas., 1031‑1044.

Hartog Jager, D.D., Giles, M.R. and Griffiths, G.R. 1993. Evolution of Paleogene submarine fans of the North Sea in space and time. Geological Society, London, Petroleum Geology Conference Series. 4 (1), 59–71. doi:10.1144/0040059.

Doughty-Jones, G., Mayall, M., & Lonergan, L. 2017. Stratigraphy, facies, and evolution of deepwater lobe complexes within a salt-controlled intraslope minibasin. AAPG Bulletin, 101(11),1879–1904. https://doi.org/10.1306/01111716046

Eldrett, J., Tripsanas, E., Davis, C., McKie, T., Vieira, M., Osterloff, P. & Sandison, T. 2015. Sedimentological Evolution of Sele Formation Deep-Marine Depositional Systems of the Central North Sea. Geological Society special publication. 403 (1), 1–3. doi:10.1144/SP403.9.

Erratt, D., Thomas, G.M. & Wall, G.R.T. 1999 The evolution of the Central North Sea Rift. Geological Society, London, Petroleum Geology Conference Series. 5 (1), 63–82. doi:10.1144/0050063.

Evans, N., Rorison, P., and Sykes, G. 1999. Banff Field, UK Central Graben – evaluation of a steeply dipping, fractured chalk reservoir. Petroleum Geology of Northwest Europe: Proceedings of the 5th Conference, 2, 975–988. https://doi.org/10.1144/0050975

Evans, D., Graham, C., Armour, A., and Bathurst, P. 2003. The Millennium Atlas: Petroleum Geology of the Central and Northern North Sea. In: Geological Society, London.

Gannaway Dalton, C.E., Giles, K.A., Munoz, ˜ J.A., Rowan, M.G., 2020a. Sedimentologic and sequence-stratigraphic characterization of salt-related basins and megaflaps at the Aulet and Adons diapirs, Spanish Pyrenees, Catalunya. Mar. Petrol. Geol. in review.

Gee, M. J. R., & Gawthorpe, R. L. 2006. Submarine channels controlled by salt tectonics: Examples from 3D seismic data offshore Angola. Marine and Petroleum Geology, 23(4), 443–458. https://doi.org/10.1016/j.marpetgeo.2006.01.002

Giles, K.A., Lawton, T.F. 2002. Halokinetic sequence stratigraphy adjacent to the El Papalote diapir, northeastern Mexico. AAPG Bull. 86, 823–840. https://doi.org/ 10.1306/61EEDBAC-173E-11D7-8645000102C1865D.

Giles, K. A. and Rowan, M.G. 2012. Concepts in halokinetic-sequence deformation and stratigraphy. Geological Society special publication 363(1): 7-31.

Glennie, K. W. (ed.) Petroleum Geology of the North Sea, Basic Concepts and Recent Advances, 4th edn. Blackwell, Oxford, 463–547.

Harrison, J.C., Jackson, M.P.A. 2014. Exposed evaporite diapirs and minibasins above a canopy in central sverdrup basin, axel heiberg Island, arctic Canada. Basin Res. 26, 567–596. https://doi.org/10.1111/bre.12037.

Haughton, P., Davis, C., McCaffrey, W., and Barker, S. 2009. Hybrid Sediment Gravity Flow Deposits – Classification, Origin and Significance.” Marine and petroleum geology 26.10: 1900–1918. Web.

Hearon, I.V., Rowan, M.G., Giles, K.A. and Hart, W.H. 2014. Halokinetic deformation adjacent to the deepwater Auger Diapir, Garden Banks 470, northern Gulf of Mexico; testing the applicability of an outcrop-based model using subsurface data. Society of Exploration Geophysicists, ISSN: 2324-8858; EISSN: 2324-8866; DOI: 10.1190/INT-2014-0053.1; Interpretation (Tulsa), Vol.2 (4), p.SM57-SM76

Hearon, T.E.I.V., Rowan, M.G., Giles, K.A., Kernen, R.A., Gannaway, C.E., Lawton, T.F., Fiduk, J.C., 2015a. Allochthonous salt initiation and advance in the northern Flinders and eastern Willouran Ranges, South Australia: using outcrops to test subsurface-based models from the northern Gulf of Mexico. AAPG Bull. 99, 293–331. https://doi.org/10.1306/08111414022.

Hearon, T.E.I.V., Rowan, M.G., Lawton, T.F., Hannah, P.T., Giles, K.A. 2015b. Geology and tectonics of Neoproterozoic salt diapirs and salt sheets in the eastern Willouran Ranges, South Australia. Basin Res. 27, 183–207. https://doi.org/10.1111/ bre.12067.

Hempton, M., Marshall, J., Sadler, S., Hogg, N., Charles, R., and Harvey, C. 2005. Turbidite Reservoirs of the Sele Formation, Central North Sea: Geological Challenges for Improving Production. Geological Society, London, Petroleum Geology Conference Series 6.1: 449–459.

Hodgson, N. A., Farnsworth, J and Fraser, A.J. 1992. Salt-Related Tectonics, Sedimentation and Hydrocarbon Plays in the Central Graben, North Sea, UKCS. Exploration Britain: Geological Insights for the Next Decade 67.1: 31–63. Web.

Jackson, M.P.A., 1995. Retrospective salt tectonics. In: Jackson, M.P.A., Roberts, D.G., Snelson, S. (Eds.), Salt Tectonics: a Global Perspective, 65. AAPG Mem, pp. 1–28. https://doi.org/10.1306/M65604.

Jackson, M. P. A. and Hudec, M.R. 2017. Salt tectonics: principles and practice. Cambridge, Cambridge University Press.

Jackson, M.P.A., and Talbot, C. J., 1991. A Glossary of Salt Tectonics: The University of Texas at Austin, Bureau of Economic Geology, Geological Circular 91-4, 44 p. doi.org/10.23867/gc9104D.

Jackson, M.P.A., Cornelius, R.R., Craig, C.H., Gansser, A., Stocklin, ¨ J., Talbot, C.J. 1990. Salt diapirs of the great kavir, Central Iran. GSA Mem 177. https://doi.org/10.1130/ MEM177.

Jennette, D.C. & Riley, C.O. 1996 Influence of relative sea-level on facies and reservoir geometry of the Middle Jurassic lower Brent Group, UK North Viking Graben. Geological Society special publication. 104 (1), 87–113. doi:10.1144/GSL.SP.1996.104.01.07.

Johnson, H.A., Bredeson, D.H., 1971. Structural development of some shallow salt domes in Louisiana Miocene productive belt. AAPG Bull. 55, 204–226. https://doi.org/ 10.1306/5D25CE19-16C1-11D7-8645000102C1865D.

Johnson, H. D. and Fisher, M. J. 1998. North Sea Plays:Geological controls on hydrocarbon distribution. In: Glennie, K. W. (ed.) Petroleum Geology of the North Sea, Basic Concepts and Recent Advances, 4th edn. Blackwell, Oxford, 463–547.

Kane, I. A., Mcgee, D. T., & Jobe, Z. R. 2012. Halokinetic effects on submarine channel equilibrium profiles and implications for facies architecture: Conceptual model illustrated with a case study from magnolia field, Gulf of Mexico. Geological Society Special Publication, 363(1),289–302. https://doi.org/10.1144/SP363.13

Kernen, R.A., Giles, K.A., Rowan, M.G., Lawton, T.F., Hearon, T.E.I.V. 2012. Depositional and halokinetic-sequence stratigraphy of the neoproterozoic wonoka formation adjacent to Patawarta allochthonous salt sheet, central Flinders ranges, south Australia. In: Alsop, G.I., Archer, S.G., Hartley, A.J., Grant, N.T., Hodgkinson, R. (Eds.), Salt Tectonics, Sediments and Prospectivity, 363. Geol. Soc. Spec. Pub., pp. 81–105. https://doi.org/10.1144/SP363.5

Kneller, B.C. 2003. The influence of flow parameters onturbidite channel slope architecture.Mar. Petrol. Geol.,20,901–910.

Lonergan, L. and Cartwright, J.A. 1999. Polygonal Faults and Their Influence on Deep-Water Sandstone Reservoir Geometries, Alba Field, United Kingdom Central North Sea AAPG Bulletin, V. 83, No. 3 P. 410–432.

Lowe, D.R. and Guy, M. 2000. Slurry-flow deposits in the Britannia Formation (Lower Cretaceous), North Sea: a new perspective on the turbidity current and debris flow problem. Sedimentology, 47, 31- 70.

Lowe, D., Guy, M., and Palfrey, A. 2003. Facies of slurry-flow deposits, Britannia Formation (Lower Cretaceous), North Sea: implications for flow evolution and deposit geometry. Sedimentology, Vol. 50, pp. 45–80. https://doi.org/10.1046/j.1365-3091.2003.00507.x

Mannie, A., Jackson, C.-L., Hampson, G. and Fraser, A. 2016. Tectonic controls on the spatial distribution and stratigraphic architecture of a net-transgressive shallow-marine syn-rift succession in a salt-influenced rift basin: Middle-to-Upper Jurassic, Norwegian Central North Sea.

Mannie, A.S., Jackson, C.A.L. and Hampson, G.J. 2014. Shallow-marine reservoir development in extensional diapir-collapse minibasins; an integrated subsurface case study from the Upper Jurassic of the Cod Terrace, Norwegian North Sea. AAPG bulletin. 98 (10), 2019–2055. doi:10.1306/03201413161.

Mayall, M., Lonergan, L., Bowman, A., James, S., Mills, K., Primmer, T., Pope, D., Rogers, L. and Skeene, R. 2010. The response of turbidite slope channels to growth-induced seabed topography. AAPG bulletin. 94 (7), 1011–1030. doi:10.1306/01051009117.

Mulder, T. and Alexander, J. 2001. The physical character of subaqueous sedimentary density flows and their deposits. Sedimentology, 48, 269-299.

Murray, 1968

Mutti, E., 1977. Distinctive thin-bedded turbidite facies and related depositional environments in the Eocene Hecho Group (South-central Pyrenees, Spain): Sedimentology, v. 24, p. 107–131

Mutti, E. and Ricci Lucchi, F. 1978. Turbidites of the northern Apennines: introduction to facies analysis. International geology review, 20, 125-166.

Oakman and Partington 1998 in Petroleum geology of the North Sea: basic concepts and recent advances. Glennie, K.W. (1998) Fourth edition. Oxford, Blackwell Science.

Oluboyo, A. P., Gawthorpe, R. L., Bakke, K., and Hadler-Jacobsen, F. 2014. Salt tectonic controls on deep-water turbidite depositional systems: Miocene, southwestern Lower Congo Basin, offshore Angola. Basin Research, 26(4), 597–620. https://doi.org/10.1111/bre.12051

Perch-Nielsen,k, Ulleberg, K and Evense, J.A 1979 Comments on the terminal Cretaceous event 106-111 in Proceedings of the Cretaceous-Tertiary boundary events symposium, Copenhagen, 1979, Vol 2 (Copenhagen:Univeristy of Copenhagen).

Pichat, A., Hoareau, G., Callot, J.-P., Ringenbach, J.-C., 2019. Characterization of oligo-miocene evaporite-rich minibasins in the Sivas Basin, Turkey. Mar. Petrol. Geol. 110, 587–605. https://doi.org/10.1016/j.marpetgeo.2019.07.050.

Pichel, L. M. and Jackson, C.A.L. 2020. Four-dimensional Variability of Composite Halokinetic Sequences. Basin research 32(6): 1277-1299.

Pickering, K., Stow, D., Watson, M. and Hiscott, R. 1986. Deep-water facies, processes arid models: a review and classification scheme for modern and ancient sediments. Earth Science Reviews, v.23, p.75-174

Pickering, K., Stow, D., Watson, M., & Hiscott, R. 1986. Deep-water facies, processes and models: a review and classification scheme for modern and ancient sediments. Earth-Science Reviews, 23(2), 75–174. https://doi.org/https://doi.org/10.1016/0012-8252(86)90001-2

Pickering, K. T., Corregidor, J., and Clark, J. D. 2015. Architecture and stacking patterns of lowerslope and proximal basin-floor channelised submarine fans, Middle Eocene Ainsa System,

Spanish Pyrenees: An integrated outcrop-subsurface study. Earth-Science Reviews, 144, 47–81. https://doi.org/10.1016/j.earscirev.2014.11.017 refer in study

Poprawski, Y., Basile, C., Jaillard, E., Gaudin, M., Lopez, M., 2016. Halokinetic sequences in carbonate systems: an example from the middle-Albian Bakio breccias formation (Basque Country, Spain). Sediment. Geol. 334, 34–52. https://doi.org/10.1016/j. sedgeo.2016.01.013.

Poprawski, Y., Basile, C., Agirrezabala, L.M., Jaillard, E., Gaudin, M., Jacquin, T., 2014. Sedimentary and structural record of the Albian growth of the Bakio salt diapir (the Basque Country, northern Spain). Basin Res. 26, 746–766. https://doi.org/10.1111/ bre.12062.

Posamentier, H.W. & Kolla, V. 2003. Seismic geomorphology and stratigraphy of depositional elements in deep-water settings. Journal of sedimentary research. 73 (3), 367–388. doi:10.1306/111302730367.

Prather, B.F. 2003. Controls on reservoir distribution, archi-tecture and stratigraphic trapping in slope settings.Mar. Pet-rol. Geol.,20, 529–545.

Prather, B.E., Booth, J.R., Steffens, G.S. and Craig, P.A. 1998. Classification, lithologic calibration and strati-graphic succession of seismic facies from intraslope basins,deep water Gulf of Mexico, USA.AAPG Bull.,82(5), 701-728.

Prather, B.E., Pirmez, C., Sylvester, Z. & Prather, D.S. 2012. Stratigraphic response to evolving geomorphology in a submarine apron perched on the upper Niger Delta slope. Application of the

principles of seismic geomorphology to continental-slope and base-of-slope systems: Case studies from seafloor and near-seafloor analogues: Society for Sedimentary Geology (SEPM) Special Publication 99, 145-161.

Ravnas, R., Nottvedt, A., Steel, R.J. & Windelstad, J. 2000 Syn-rift sedimentary architectures in the Northern North Sea. Dynamics of the Norwegian Margin. 167 (1), 133–177. doi:10.1144/GSL.SP.2000.167.01.07.

Ravnås, R. & Steel, R.J. 1997. Contrasting styles of Late Jurassic syn-rift turbidite sedimentation: a comparative study of the Magnus and Oseberg areas, northern North Sea. Marine and Petroleum Geology, 14, 417-449.

Rodriguez, C., Jackson, C., Bell, R., Rotevatn, A., and Francis, M. 2019. Deep-water reservoir distribution on a salt-influenced slope, Santos Basin, offshore Brazil. https://doi.org/10.31223/osf.io/8v6x7

Rojo, L.A., Escalona, A., 2018. Controls on minibasin infill in the Nordkapp basin: evidence of complex Triassic synsedimentary deposition influenced by salt tectonics. AAPG Bull. 102, 1239–1272. https://doi.org/10.1306/0926171524316523.

Rojo, L.A., Escalona, A., Schulte, L. 2016. The use of seismic attributes to enhance imaging of salt structures in the Barents Sea. First Break 34, 49–57. https://doi.org/ 10.3997/1365-2397-2016014.

Rowan, M.G., Ratliff, R.A., 2012. Cross-section restoration of salt-related deformation: best practices and potential pitfalls. J. Struct. Geol. 41, 24–37. https://doi.org/ 10.1016/j.jsg.2011.12.012.

Rowan, M.G., Lawton, T.F., Giles, K.A., Ratliff, R.A. 2003. Near-salt deformation in La Popa basin, Mexico, and the northern Gulf of Mexico: a general model for passive diapirism. AAPG Bull. 87, 733–756. https://doi.org/10.1306/01150302012.

Rowan, M.G., Giles, K.A., Hearon, T.E.I.V., Fiduk, J.C. 2016. Megaflaps adjacent to salt diapirs.AAPG Bull. 100, 1723–1747. https://doi.org/10.1306/05241616009.

Rowan, M.G., Muñoz, J.A., Giles, K.A., Roca, E., Hearon, T.E., Fiduk, J.C., Ferrer, O. and Fischer, M.P. 2020. Folding and fracturing of rocks adjacent to salt diapirs. Journal of structural geology. 141, 104187–. doi:10.1016/j.jsg.2020.104187.

Saura, E., Ard`evol i Oro, ´ L., Teixell, A., Verg´es, J., 2016. Rising and falling diapirs, shifting depocenters, and flap overturning in the Cretaceous Sopeira and Sant Gerv` as subbasins (Ribagorça Basin, southern Pyrenees). Tectonics 35. https://doi.org/ 10.1002/2015TC004001.

Saura, E., Verg´es, J., Martín-Martín, J.D., Messager, G., Moragas, M., Razin, P., Gr´elaud, C., Joussiaume, R., Malaval, M., Homke, S., Hunt, D.W., 2014. Syn- to postrift diapirism and minibasins of the Central High Atlas (Morocco): the changing face of a mountain belt. J. Geol. Soc. 171, 97–105. https://doi.org/10.1144/jgs2013-079.

Schultz-Ela, D.D. 2003. Origin of drag folds bordering salt diapirs. AAPG Bull. 87, 757–780. https://doi.org/10.1306/12200201093.

Schultz-Ela, D.D., Jackson, M.P.A., Vendeville, B.C., 1993. Mechanics of active salt diapirism. Tectonophysics 228, 275–312. https://doi.org/10.1016/0040-1951(93) 90345-K.

Scott, E.D., Gelin, F., Jolley, S.J., Leenaarts, E., Sadler, S.P., and Elsinger, R.J., 2010, Sedimentological control of fluid flow in deep marine turbidite reservoirs: Pierce Field, UK Central North Sea, in Jolley, S.J., Fisher, Q.J., Ainsworth, R.B., Vrolijk, P.J., and Delisle, S., eds., Reservoir Compartmentalization: Geological Society of London, Special Publication 347, p. 113–132.

Shanmugam, G. (Ganapathy). 2006. Deep-Water Processes and Facies Models Implications for Sandstone Petroleum Reservoirs. Amsterdam ;: Elsevier, Print. (1944) refer to this

Simon-Robertson, 1992. A sedimentological study of well UK 23/27-9.

Smith, R. 2004. Silled sub-basins to connected tortuous corri-dors: sediment distribution systems on topographically com-plex sub-aqueous slopes. In:Confined Turbidite Systems (Ed.by S.A. Lomas & P. Joseph) Geol. Soc. London Spec. Publ., 222, 23-44.

Snidero, M., Munoz, ˜ J.A., Carrera, N., Butill´e, M., Mencos, J., Motamedi, H., Piryaei, A., S` abat, F., 2019. Temporal evolution of the Darmadan salt diapir, eastern Fars region, Iran. Tectonophysics 766, 115–130. https://doi.org/10.1016/j.tecto.2019.06.006.

Stevenson, C.J., Peakall, J., Hodgson, D.M., Bell, D. and Privat, A. 2020. TB or not TB; banding in turbidite sandstones. Journal of sedimentary research. 90 (8), 821–842. doi:10.2110/jsr.2020.43.

Stewart, S.A., 2006. Implications of passive salt diapir kinematics for reservoir segmentation by radial and concentric faults. Mar. Petrol. Geol. 23, 843–853.

Stow, D. A. V., and M. Johansson, 2000, Deepwater massive sands: Nature, origin and hydrocarbon implications: Marine and Petroleum Geology, v. 17, p. 145–174.

Stow, D. A. V., and Omoniyi, B. A., 2018. Thin-bedded turbidites: Overview and petroleum perspective, in C. C. Turner and B. T. Cronin, eds., Rift-related coarse-grained submarine fan reservoirs; the Brae Play, South Viking Graben, North Sea: AAPG Memoir 115, p. 97–118

Stow, D.A.V. & Shanmugam, G. 1980 Sequence of structures in fine-grained turbidites: Comparison of recent deep-sea and ancient flysch sediments. Sedimentary geology. 25 (1), 23–42. doi:10.1016/0037-0738(80)90052-4.

Sylvester, Z. & Lowe, D.R. 2004 Textural trends in turbidites and slurry beds from the Oligocene flysch of the East Carpathians, Romania. Sedimentology. 51 (5), 945–972. doi:10.1111/j.1365-3091.2004.00653.x.

Talling, P., Amy, L.A., Wynn, R., Peakall, J. and Robinson, M. 2004. Beds comprising debrite sandwiched within co-genetic turbidite: origin and widespread occurrence in distal depositional environments. Sedimentology, 51, 163-194.

Talling, P.J., Masson, D.G., Sumner, E.J. and Malgesini, G. 2012. Subaqueous sediment density flows: Depositional processes and deposit types. Sedimentology, 59, 1937-2003.

Vendeville, B.C. & Jackson, M.P.A. 1992 The rise of diapirs during thin-skinned extension. Marine and petroleum geology. 9 (4), 331–354. doi:10.1016/0264-8172(92)90047-I.

Vendeville, B. C., and Nilsen, K. T., 1995, Episodic growth of salt diapirs driven by horizontal shortening, in: Travis, C. J., Vendeville, B. C., Harrison, Holly, Peel, F. J., Hudec, M. R., and Perkins, B. F., eds., Salt, Sediment, and Hydrocarbons, Society of Economic Paleontologists and Mineralogists, Gulf Coast Section, 16th Annual Research Conference Program and Extended Abstracts, pp. 285-295.

Verg´es, J., Poprawski, Y., Almar, Y., Drzewiecki, P.A., Moragas, M., Bover-Arnal, T., Macchiavelli, C., Wright, W., Messager, G., Embry, J.-C., Hunt, D. 2020. Tectonosedimentary evolution of jurassic-cretaceous diapiric structures: miravete anticline, maestrat basin, Spain. Basin Res. https://doi.org/10.1111/bre.12447.

Wallace, W.E., 1944. Structure of South Louisiana deep-seated domes. AAPG Bull. 28, 1249–1312. https://doi.org/10.1306/3D9336B0-16B1-11D7-8645000102C1865D.

Watts, N.L., Lapre, J.F., van=Schijndel-Goester, F.S. & Ford, A. 1980 Upper Cretaceous and lower Tertiary chalks of the Albuskjell area, North Sea; deposition in a slope and a base-of-slope environment. Geology (Boulder). 8 (5), 217–221. doi:10.1130/0091-7613(1980)82.0.CO;2.

Ziegler, P. A. 1975. The Geological Evolution of the North Sea Area in the Tectonic Framework of North Western Europe. Norges Geol, (316), 1–27.

Figure captions

Figure 1. Location of the study area and bathymetric map of the North Sea showing the Pierce Field, offshore North Sea (Smith and Sandwell 1997). The Pierce Field is located in blocks 23/22a and 23/27 of the UK Continental Shelf of the North Sea. An outline of the 3D time seismic survey is represented by the green rectangle. Field outlines are coloured green, red and yellow to represent oil, gas and condensate fields.

Figure 2. Map of the principal structural elements of the Central North Sea, highlighting the main Jurassic depocentres (modified after Erratt et al. 1999, Charles and Ryzhikov 2015).

Figure 3. Well section window displaying seismic-to-well tie from well 23/27-7. Sonic and density curves are used to generate the Acoustic impedance (AI) and Reflection coefficient (RC) curves. RC is convolved with the wavelet to generate a synthetic seismogram which is compared to the seismic at the well location. Note position of well markers overlayed on well section window; only the Early Eocene (Balder Formation), top Danian Ekofisk Formation and Top Forties Sandstone Member are seismically picked. Note the high amplitude seismic expression of the top Forties Sandstone Member.

Figure 4a. 3D time -migrated profiles of South and North Pierce salt stocks, East Central Graben, North Sea. Green lines define folded sequences identified as tapered or tabular CHS using seismically imaged data. White dashed lines are axial traces of halokinetic folds. Vertical exaggeration 1.5:1 Seismic data courtesy of PGS.

Figure 4b. 2D map (2500 ms TWT time slice) illustrating the locations of W-E and N-S oriented lines displayed in fig. 6a.

Figure 4c. Schematic of a) hook halokinetic sequence, b) wedge halokinetic sequence, c) tabular composite halokinetic sequence d) tapered composite halokinetic sequence; that illustrates the different drape-fold geometries and degree of angular discordance at the bounding unconformities. (Redrawn from Jackson and Hudec, 2017)

Figure 5. Isopach maps for the six key units. a) Unit 6 BCU to Ekofisk, b) Unit 5 Ekofisk to Balder, c) Unit 4 Balder to Oligocene, d) Unit 3 Oligocene to MMU, e) Unit 2 MMU to Pleistocene, f) Unit 1 Pleistocene to Seabed.

Figure 6a. Interpreted N-S geoseismic section of the South Pierce diapir showing key overburden interpretation (units 1-6).

Figure 6b. Map showing a time slice at 3500 ms TWT and positions of several W-E and N-S oriented lines (Figs. 6a, 8 and 10).

Figure 7. Petrophysical log suite from well 23/27-10 and 23/27-9 summarizing the key formations: from left to right: GR, gamma-ray: CALI, caliper; DT, compressional (sonic) velocity; RHOB, bulk density; NPHI, neutron porosity. (SSTVD). The wells flattened on the early Eocene (Balder Formation). The cross section shows the Forties sandstone thickness changes considerably from 23/27-9 to 23/27-7 and the position of the South Pierce diapir is a controlling factor on the thickness changes from North to South. 23/27-7 shows the thickest sand accumulation of all the wells.

Figure 8. Interpreted W-E geoseismic section of North and South Pierce diapirs showing key overburden interpretation (units 1-6).

Figure 9a. Petrophysical log suite from well 23/22a-3, 23/27-9 and 23/27-5 summarizing the key formations: from left to right: GR, gamma-ray: CALI, caliper; DT, compressional (sonic) velocity; RHOB, bulk density; NPHI, neutron porosity. (SSTVD) Balder, Ekofisk formations and the top Forties Sandstone Member are seismically mapped.

Figure 9b. Pie Chart illustrating facies proportions in the cored interval from well 23/22a-3, 23/27-9 and 23/27-5 in the Forties Sandstone Member.

Figure 10. Interpreted W-E geoseismic section of North Pierce diapir showing key overburden interpretation (units 1-6).

Figure 11. Petrophysical log suite from well 23/22a-2, 23/22a-2z and 2322a-3 summarizing the key formations: from left to right: GR, gamma-ray: CALI, caliper; DT, compressional (sonic) velocity; RHOB, bulk density; NPHI, neutron porosity.

Figure 12. Summary of thick-bedded sandstones (F1) rapidly deposited from high-density turbidity currents. The dish structures and dewatering pipes are due to the post-depositional escape of water from the sand.

Figure 13. Summary of thin-bedded sandstones (F2)

Figure 14. Summary of banded sandstones (F3)

Figure 15. Summary of hybrid beds (F4)

Figure 16. Summary of slurry beds (F5)

Figure 17. Summary of debrites (F6)

Figure 18. Summary of deformation in the Tor Formation (23/22a-2) a, b) illustrates multiple high angle fractures and c) illustrates a large fracture zone that might have formed from multiple phases of fracture opening.

Figure 19. Summary of deformation in the Ekofisk Formation, a) illustrates conformable contact between Maureen Formation mudstones and chalk, b) shows an irregular subarkosic sandstone dyke fill and irregular chert nodules. Enlarged photos to the right are taken from the sedimentological study of well 23/27-9 (Simon Robertson, 1992).

Figure 20. Lateral variations in facies due to diapir growth illustrating the proportion and distribution of facies interpreted to indicate remobilisation due to diapir growth.

Table 1. Regional stratigraphy of the Central Graben, North Sea. North Sea stratigraphic nomenclature based on Knox & Cordey (1992).

Table 2. Summary of sedimentary facies from the Forties Sandstone Member and Ekofisk Formation, Pierce Field, Central North Sea

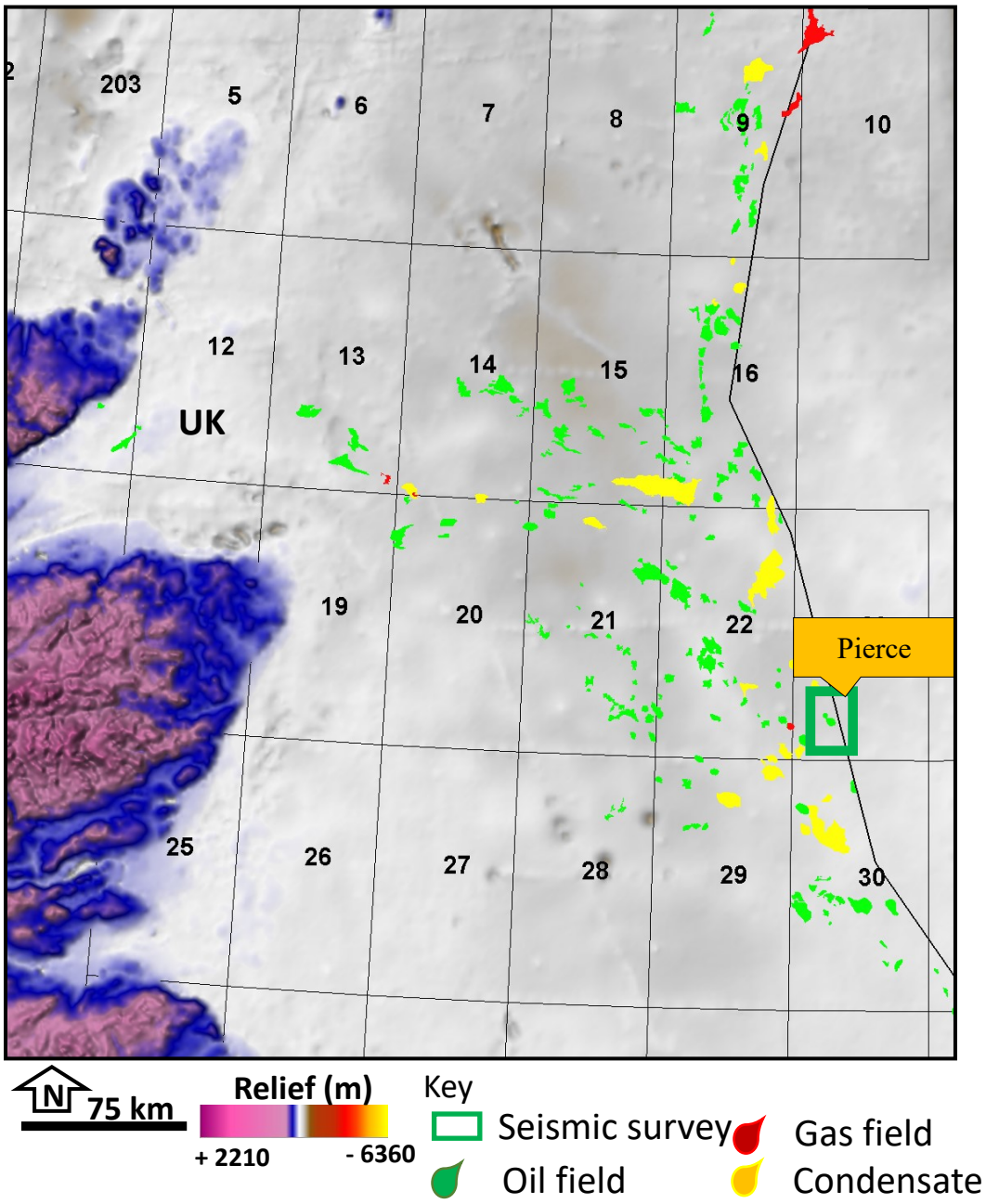
203
5
6
7
8
9
10
12
13
14
15
16
UK
19
20
21
22
Pierce
25
26
27
28
29
30
N
75 km
Relief (m)
+ 2210
- 6360
Key
Seismic survey
Gas field
Oil field
Condensate

Figure 1.

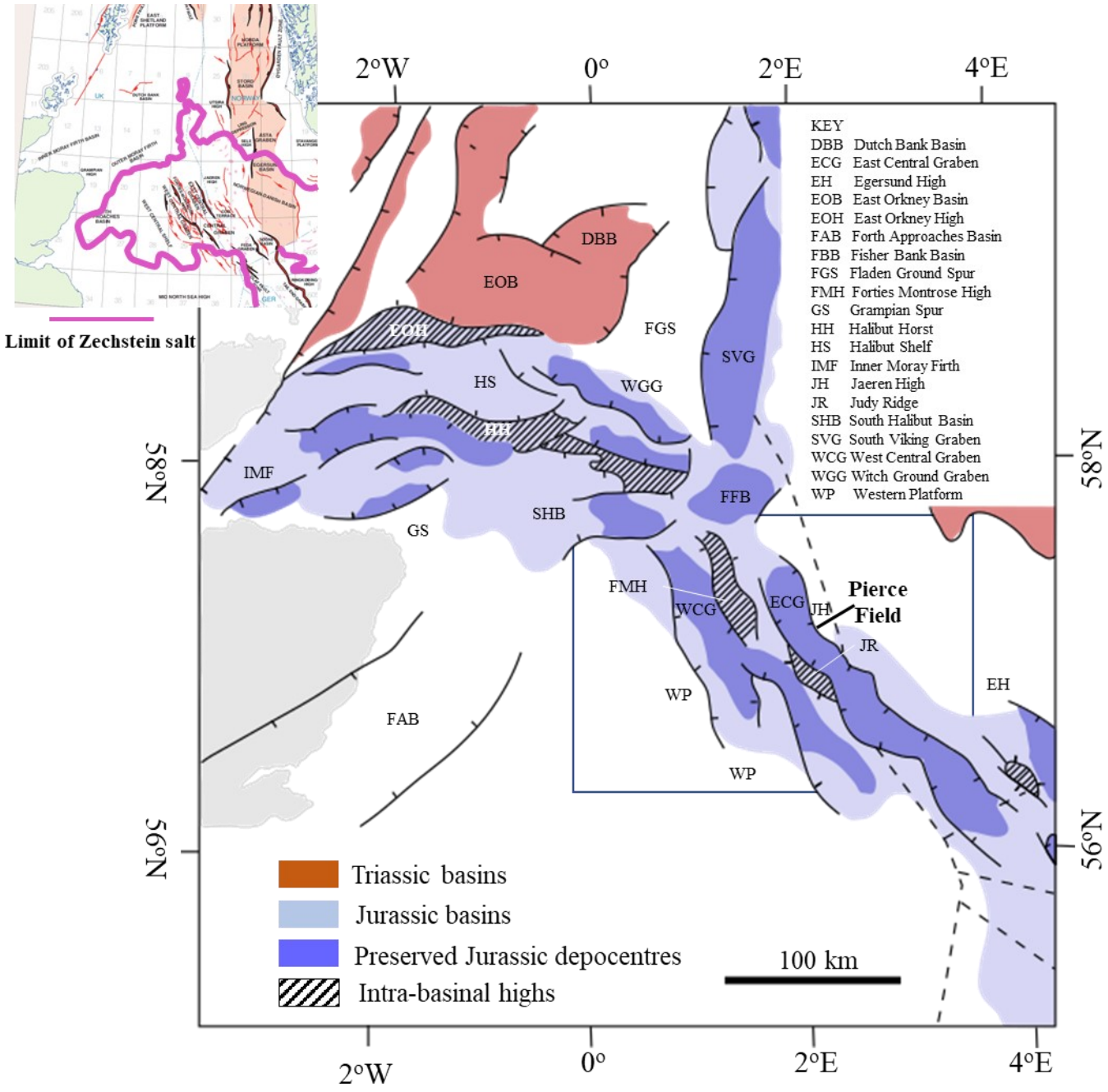
Limit of Zechstein salt
2°W
0°
2°E
4°E
58°N
56°N
KEY
DBB Dutch Bank Basin
ECG East Central Graben
EH Egersund High
EOB East Orkney Basin
EOH East Orkney High
FAB Forth Approaches Basin
FBB Fisher Bank Basin
FGS Fladen Ground Spur
FMH Forties Montrose High
GS Grampian Spur
HH Halibut Horst
HS Halibut Shelf
IMF Inner Moray Firth
JH Jaeren High
JR Judy Ridge
SHB South Halibut Basin
SVG South Viking Graben
WCG West Central Graben
WGG Witch Ground Graben
WP Western Platform
DBB
EOB
EOH
FGS
SVG
HS
WGG
HH
IMF
FFB
SHB
GS
FMH
WCG
ECG
JH
Pierce Field
JR
EH
WP
WP
FAB
Triassic basins
Jurassic basins
Preserved Jurassic depocentres
Intra-basinal highs
100 km

Figure 2.

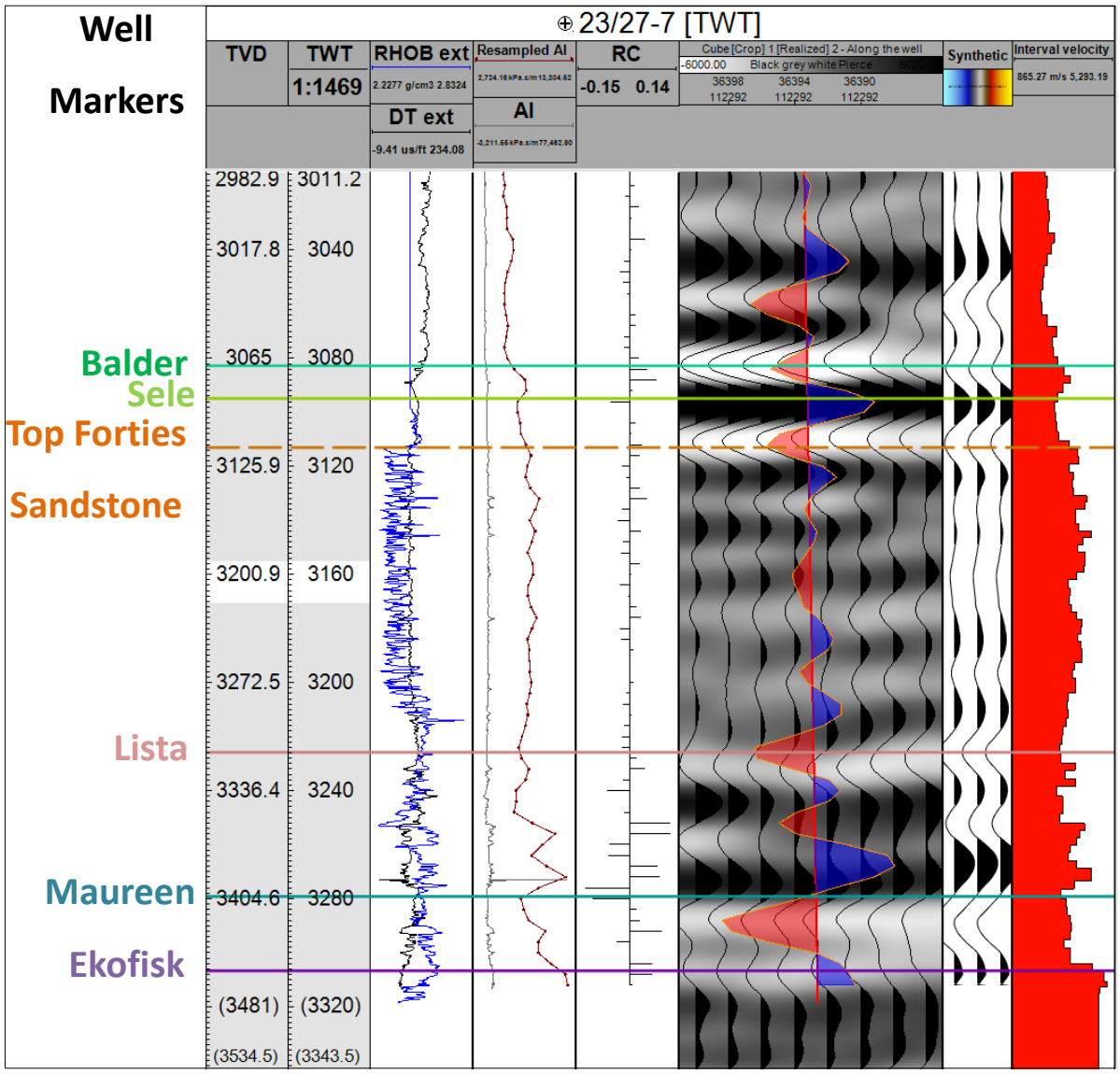
Well
Markers
⊕ 23/27-7 [TWT]
TVD
TWT
1:1469
RHOB ext
2.2277 g/cm3 2.8324
DT ext
-9.41 us/ft 234.08
Resampled AI
AI
RC
-0.15 0.14
Cube [Crop] 1 [Realized] 2 - Along the well
-6000.00 Black grey white Pierce
36398 36394 36390
112292 112292 112292
Synthetic
Interval velocity
865.27 m/s 5,293.19
2982.9
3011.2
3017.8
3040
3065
3080
Balder
Sele
Top Forties
3125.9
3120
Sandstone
3200.9
3160
3272.5
3200
Lista
3336.4
3240
Maureen
3404.6
3280
Ekofisk
(3481)
(3320)
(3534.5)
(3343.5)

Figure 3.

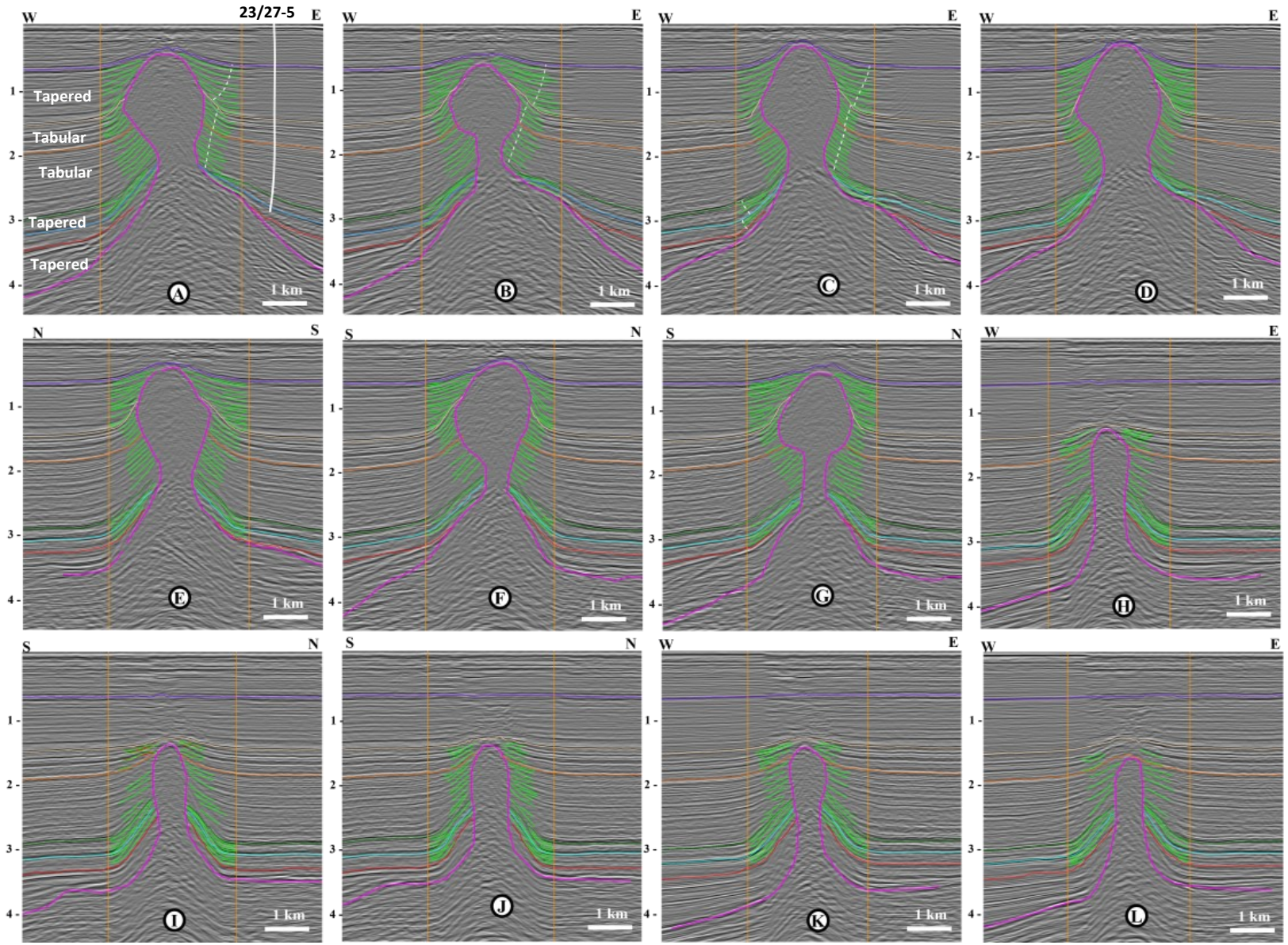
23/27-5
W
E
N
S
Tapered
Tabular
Tabular
Tapered
Tapered
1 km
A
B
C
D
E
F
G
H
I
J
K
L
1
2
3
4
Near Pleistocene
Mid Miocene Unconformity
Oligocene
Balder
Ekofisk
Base Cretaceous Unconformity
Fold
Axial trace
23/27-5

Figure 4a.

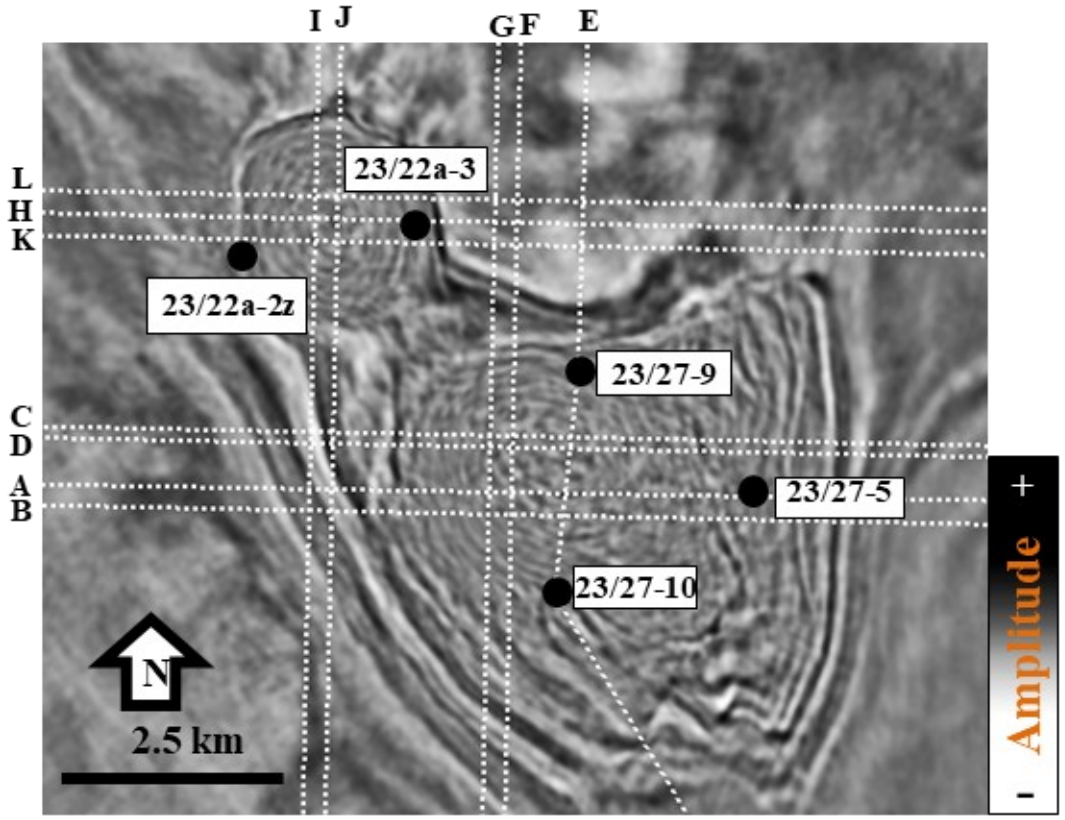

Figure 4b.

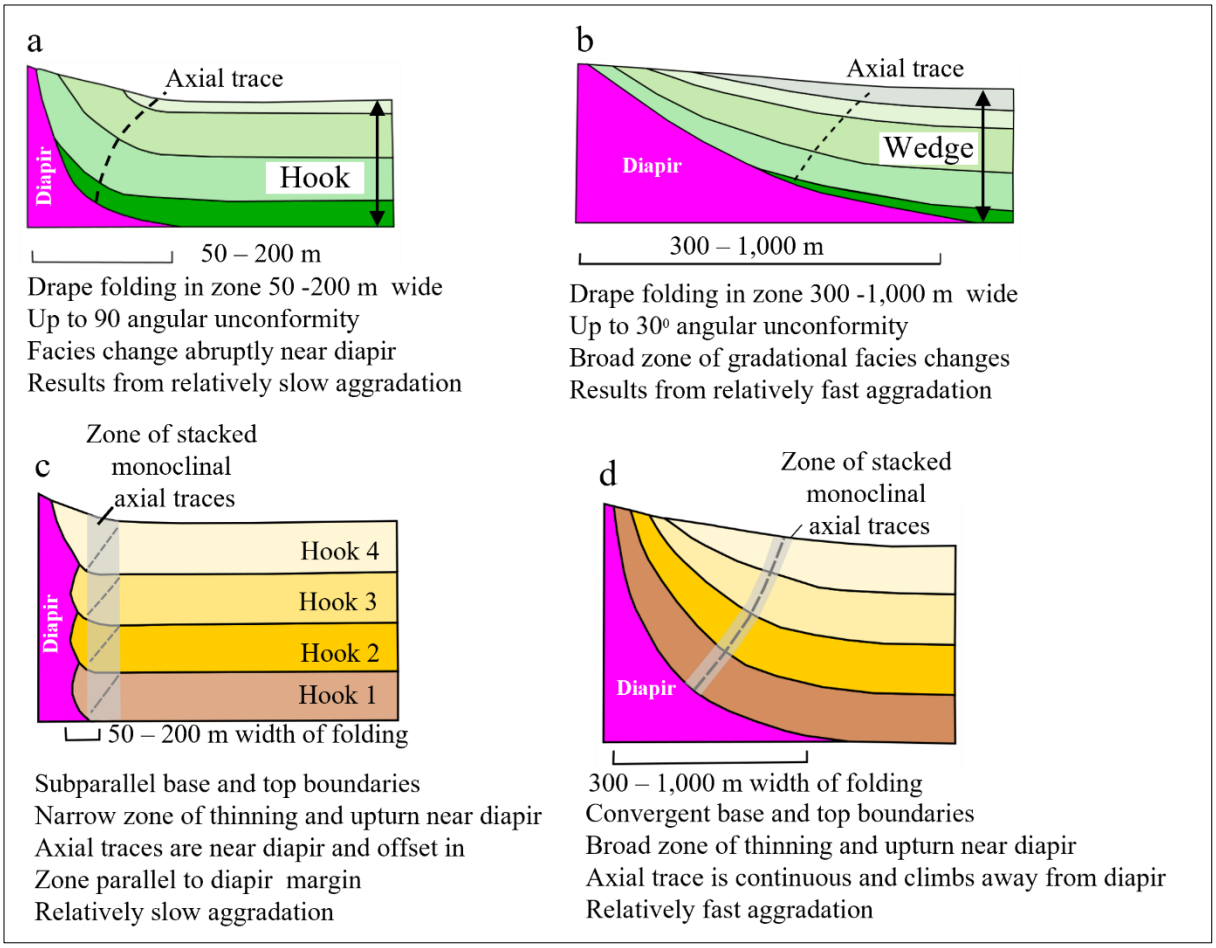
a
Axial trace
Diapir
Hook
50 – 200 m
Drape folding in zone 50 -200 m wide
Up to 90 angular unconformity
Facies change abruptly near diapir
Results from relatively slow aggradation
b
Axial trace
Diapir
Wedge
300 – 1,000 m
Drape folding in zone 300 -1,000 m wide
Up to 30⁰ angular unconformity
Broad zone of gradational facies changes
Results from relatively fast aggradation
c
Zone of stacked
monoclinal
axial traces
Diapir
Hook 4
Hook 3
Hook 2
Hook 1
50 – 200 m width of folding
Subparallel base and top boundaries
Narrow zone of thinning and upturn near diapir
Axial traces are near diapir and offset in
Zone parallel to diapir margin
Relatively slow aggradation
d
Zone of stacked
monoclinal
axial traces
Diapir
300 – 1,000 m width of folding
Convergent base and top boundaries
Broad zone of thinning and upturn near diapir
Axial trace is continuous and climbs away from diapir
Relatively fast aggradation

Figure 4c.

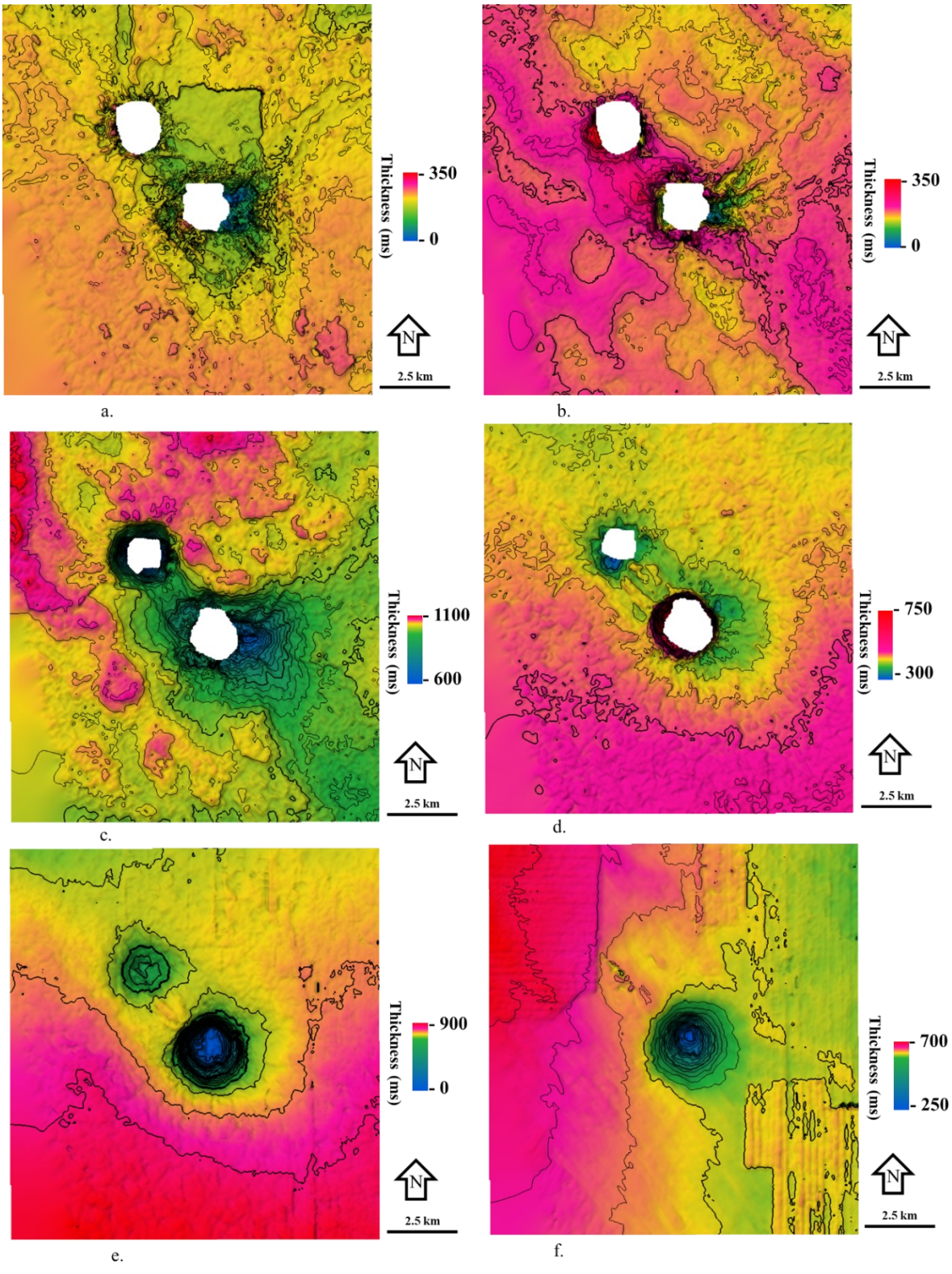
Thickness (ms)
350
0
N
2.5 km
a.
Thickness (ms)
350
0
N
2.5 km
b.
Thickness (ms)
1100
600
N
2.5 km
c.
Thickness (ms)
750
300
N
2.5 km
d.
Thickness (ms)
900
0
N
2.5 km
e.
Thickness (ms)
700
250
N
2.5 km
f.

Figure 5.

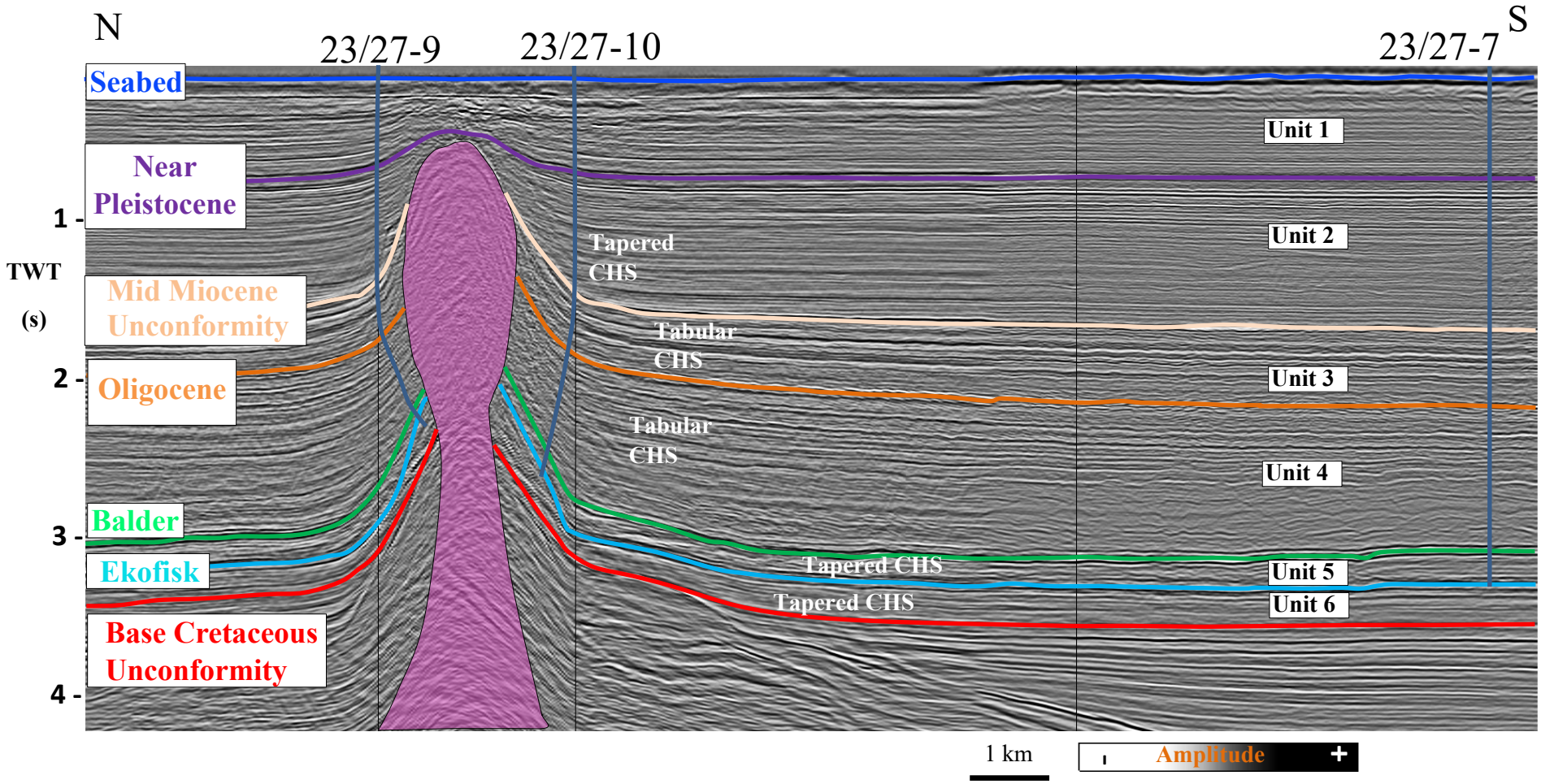
N
S
23/27-9
23/27-10
23/27-7
Seabed
Near Pleistocene
Mid Miocene Unconformity
Oligocene
Balder
Ekofisk
Base Cretaceous Unconformity
TWT (s)
1
2
3
4
Tapered CHS
Tabular CHS
Tabular CHS
Tapered CHS
Tapered CHS
Unit 1
Unit 2
Unit 3
Unit 4
Unit 5
Unit 6
1 km
Amplitude
+

Figure 6a.

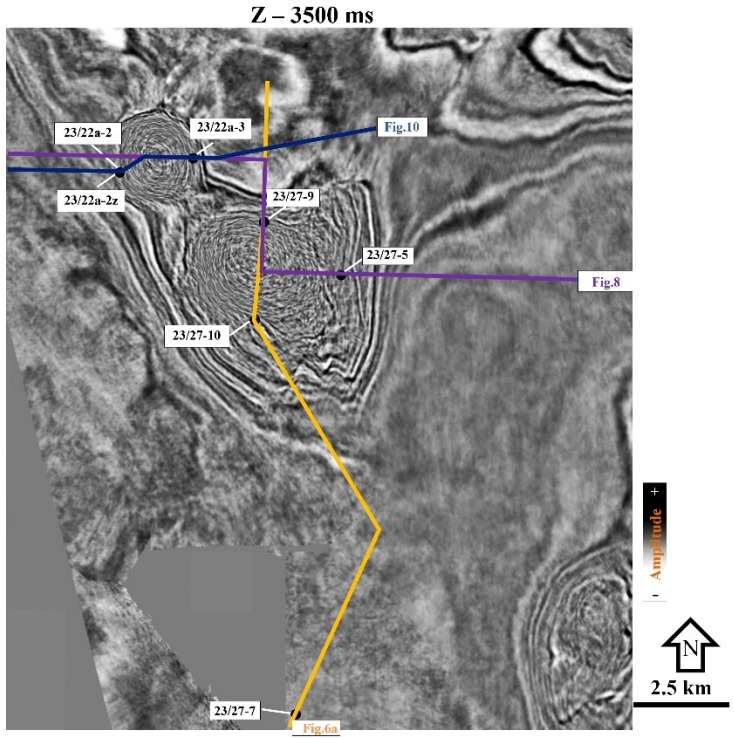
Z – 3500 ms
23/22a-2
23/22a-3
Fig.10
23/22a-2z
23/27-9
23/27-5
Fig.8
23/27-10
23/27-7
Fig.6a
Amplitude
+
-
N
2.5 km

Figure 6b.

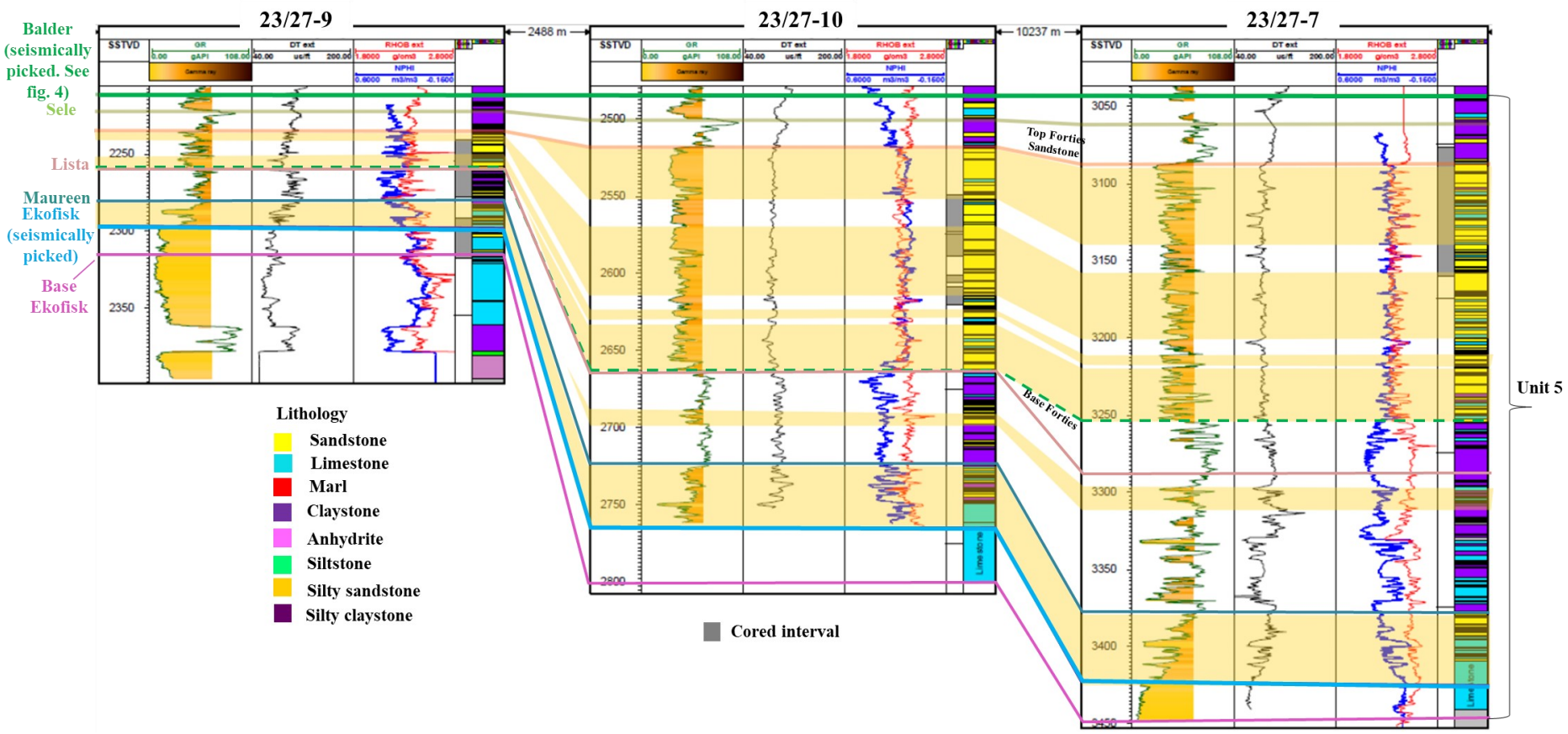
23/27-9
23/27-10
23/27-7
2488 m
10237 m
Balder (seismically picked. See fig. 4)
Sele
Lista
Maureen
Ekofisk (seismically picked)
Base Ekofisk
Top Forties Sandstone
Base Forties
Unit 5
Lithology
Sandstone
Limestone
Marl
Claystone
Anhydrite
Siltstone
Silty sandstone
Silty claystone
Cored interval

Figure 7.

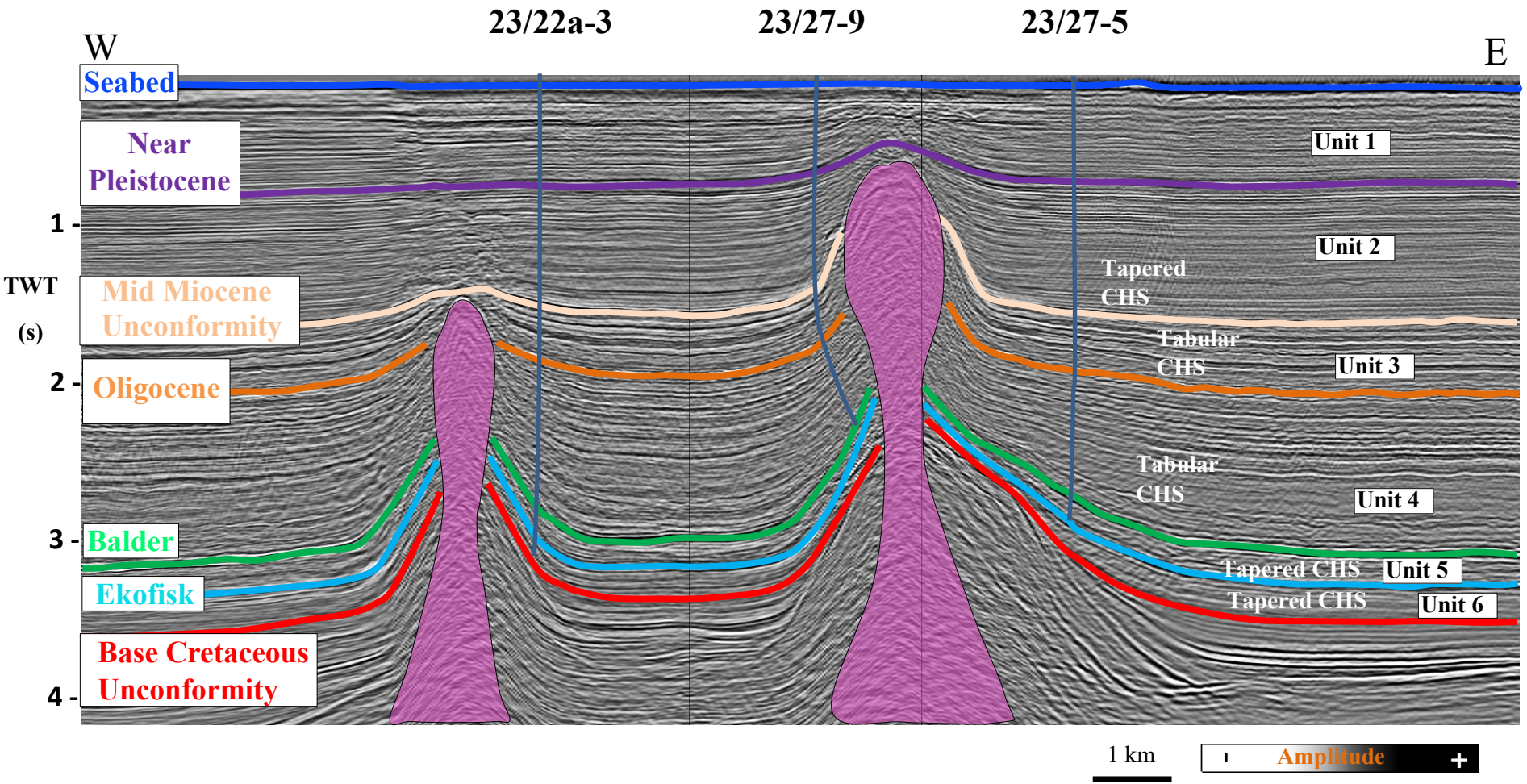
23/22a-3
23/27-9
23/27-5
W
E
Seabed
Near Pleistocene
Mid Miocene Unconformity
Oligocene
Balder
Ekofisk
Base Cretaceous Unconformity
TWT (s)
1
2
3
4
Unit 1
Unit 2
Tapered CHS
Tabular CHS
Unit 3
Tabular CHS
Unit 4
Tapered CHS
Unit 5
Tapered CHS
Unit 6
1 km
Amplitude
+

Figure 8.

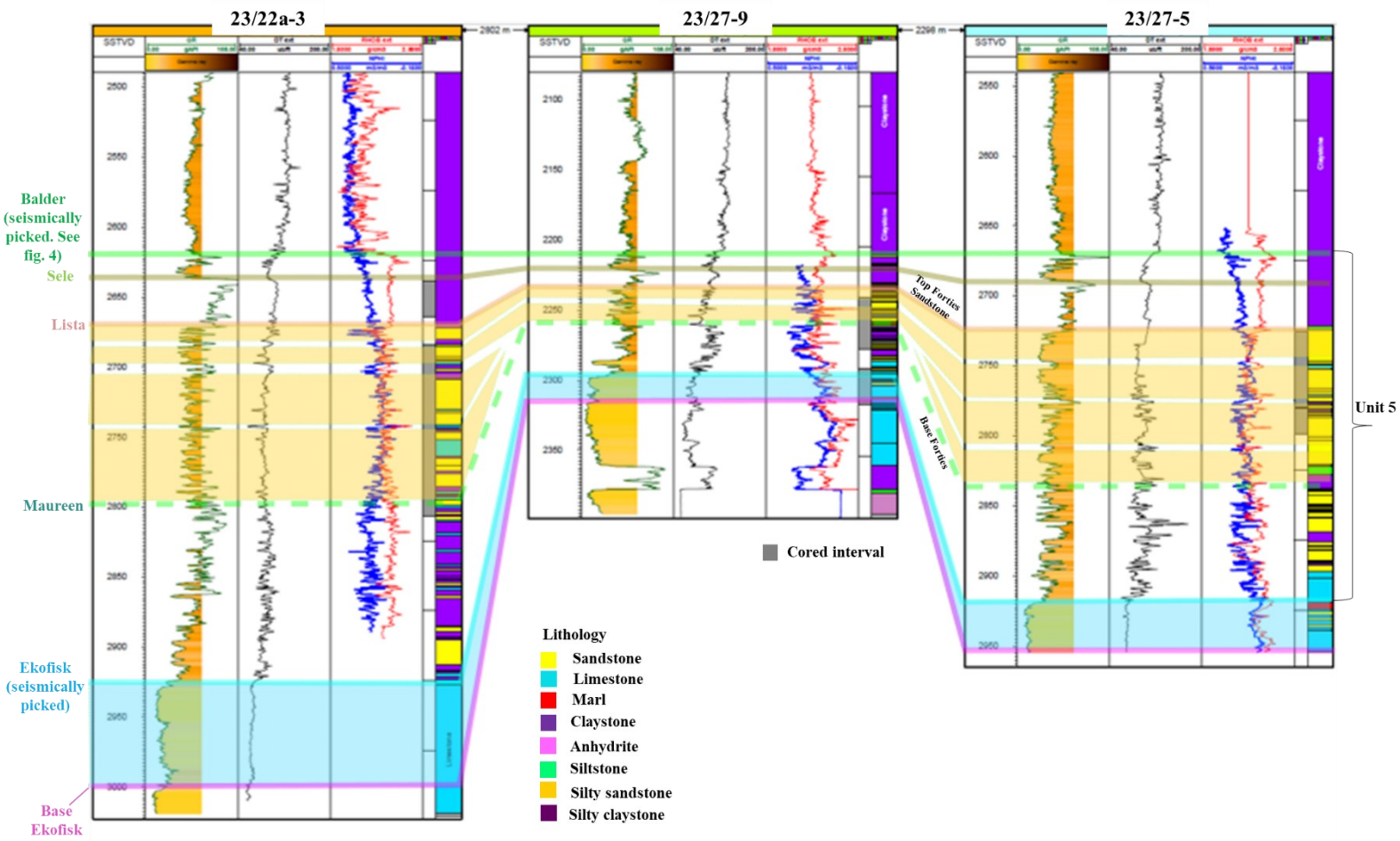
23/22a-3
23/27-9
23/27-5
Balder (seismically picked. See fig. 4)
Sele
Lista
Maureen
Ekofisk (seismically picked)
Base Ekofisk
Top Forties Sandstone
Base Forties
Unit 5
Cored interval
Lithology
Sandstone
Limestone
Marl
Claystone
Anhydrite
Siltstone
Silty sandstone
Silty claystone

Figure 9a.

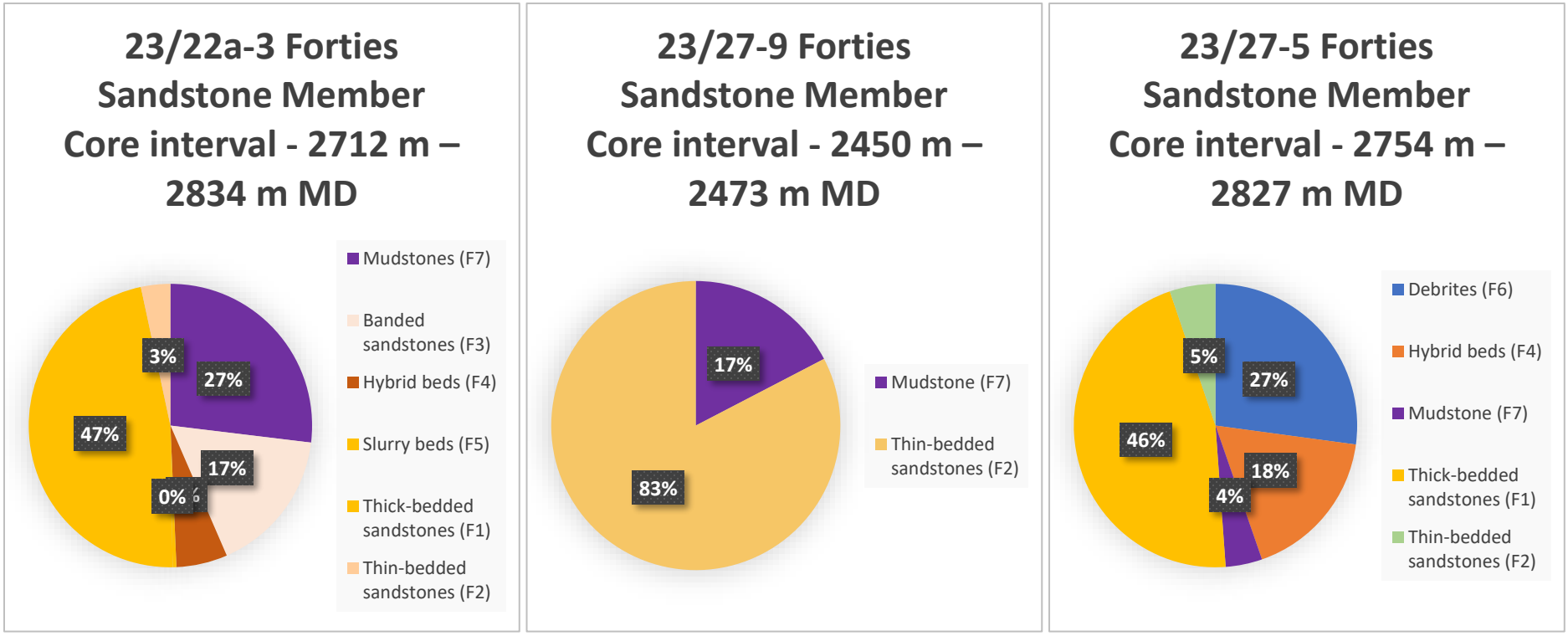
23/22a-3 Forties Sandstone Member Core interval - 2712 m – 2834 m MD
3%
27%
47%
17%
0%
Mudstones (F7)
Banded sandstones (F3)
Hybrid beds (F4)
Slurry beds (F5)
Thick-bedded sandstones (F1)
Thin-bedded sandstones (F2)
23/27-9 Forties Sandstone Member Core interval - 2450 m – 2473 m MD
17%
83%
Mudstone (F7)
Thin-bedded sandstones (F2)
23/27-5 Forties Sandstone Member Core interval - 2754 m – 2827 m MD
5%
27%
46%
18%
4%
Debrites (F6)
Hybrid beds (F4)
Mudstone (F7)
Thick-bedded sandstones (F1)
Thin-bedded sandstones (F2)

Figure 9b.

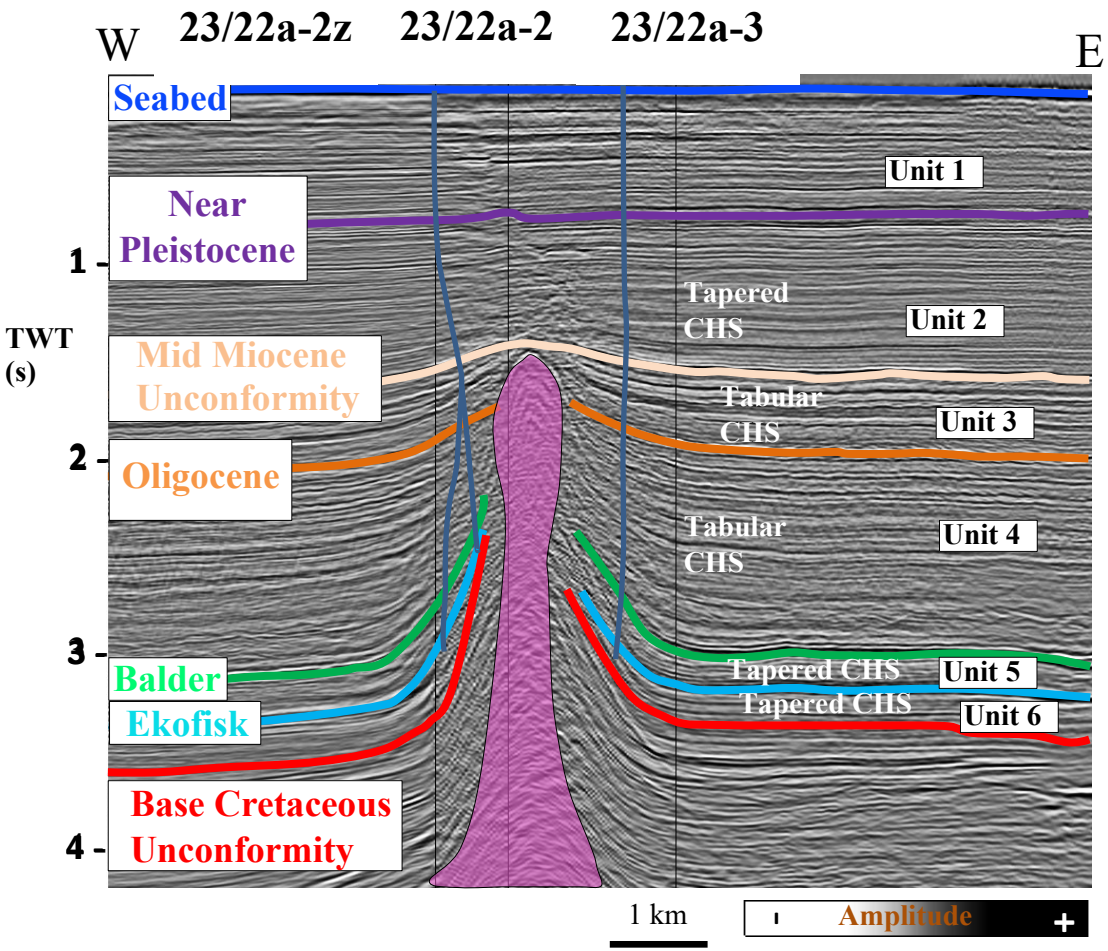
W
23/22a-2z
23/22a-2
23/22a-3
E
Seabed
Near Pleistocene
Mid Miocene Unconformity
Oligocene
Balder
Ekofisk
Base Cretaceous Unconformity
TWT (s)
1
2
3
4
Unit 1
Tapered CHS
Unit 2
Tabular CHS
Unit 3
Tabular CHS
Unit 4
Tapered CHS
Unit 5
Tapered CHS
Unit 6
1 km
Amplitude
+

Figure 10.

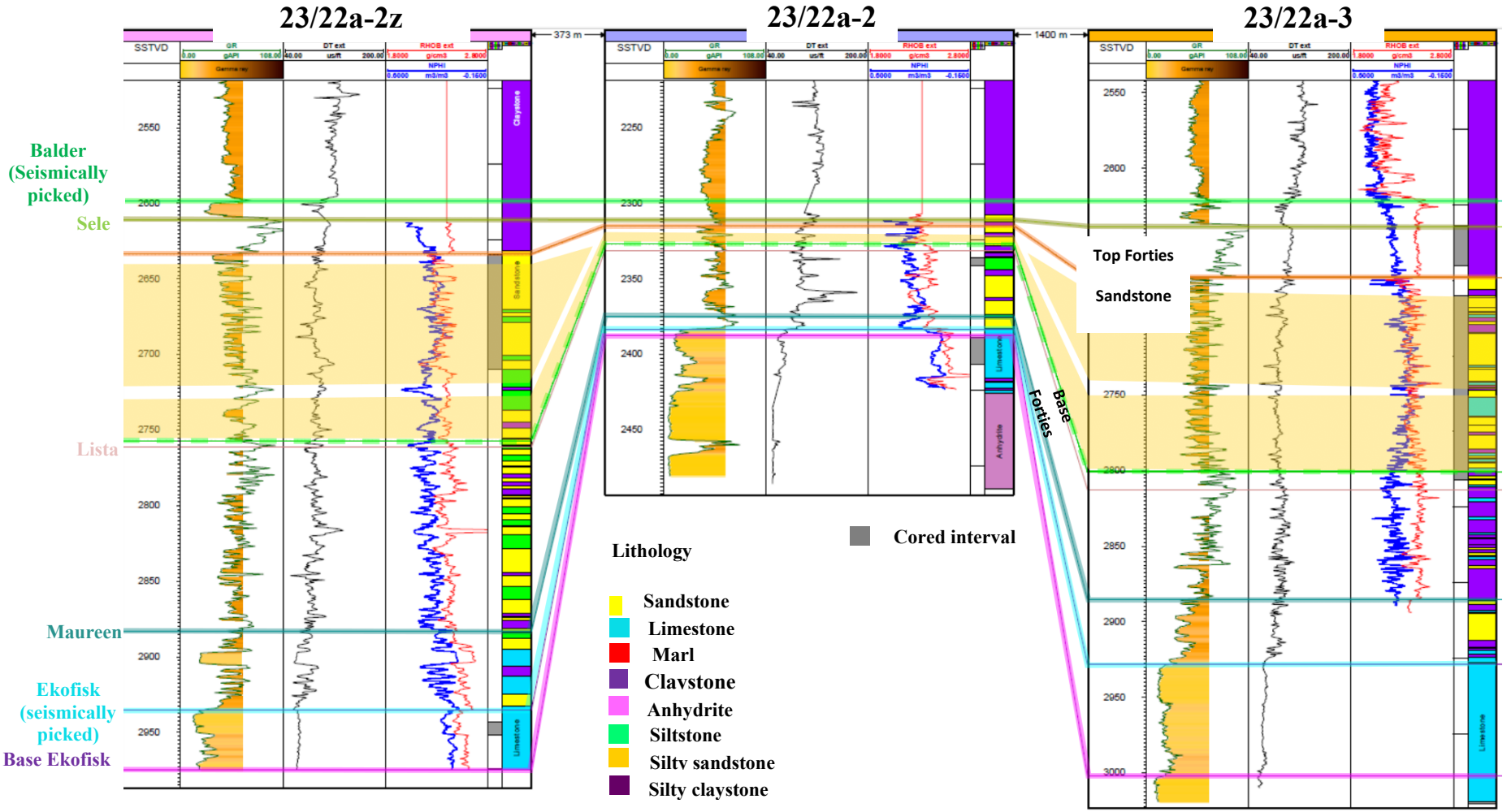
23/22a-2z
23/22a-2
23/22a-3
373 m
1400 m
Balder
(Seismically
picked)
Sele
Lista
Maureen
Ekofisk
(seismically
picked)
Base Ekofisk
Top Forties
Sandstone
Base
Forties
Lithology
Sandstone
Limestone
Marl
Clavstone
Anhydrite
Siltstone
Silty sandstone
Silty claystone
Cored interval

Figure 11.

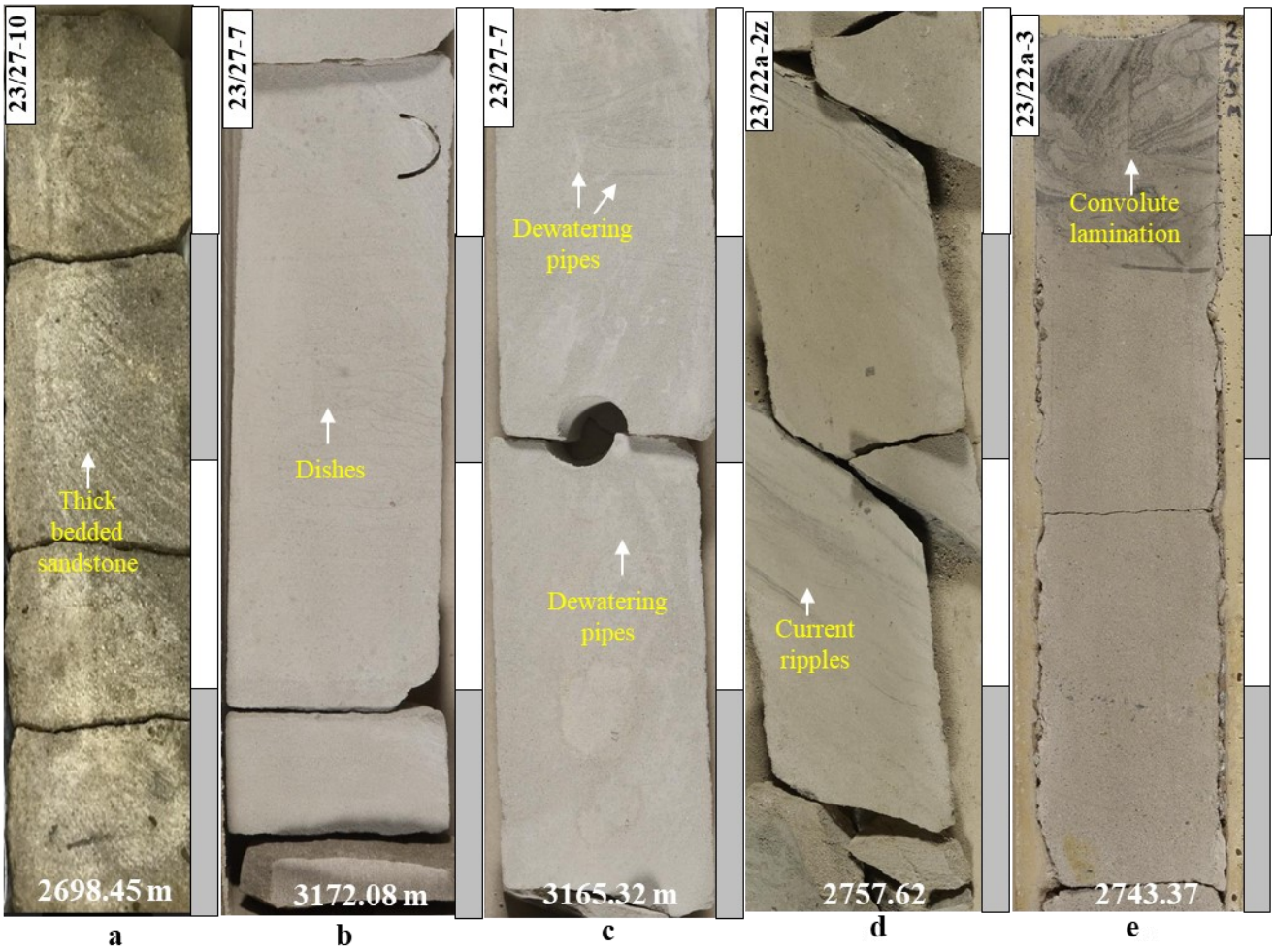
23/27-10
Thick bedded sandstone
2698.45 m
a
23/27-7
Dishes
3172.08 m
b
23/27-7
Dewatering pipes
Dewatering pipes
3165.32 m
c
23/22a-2z
Current ripples
2757.62
d
23/22a-3
Convolute lamination
2743.37
e

Figure 12.

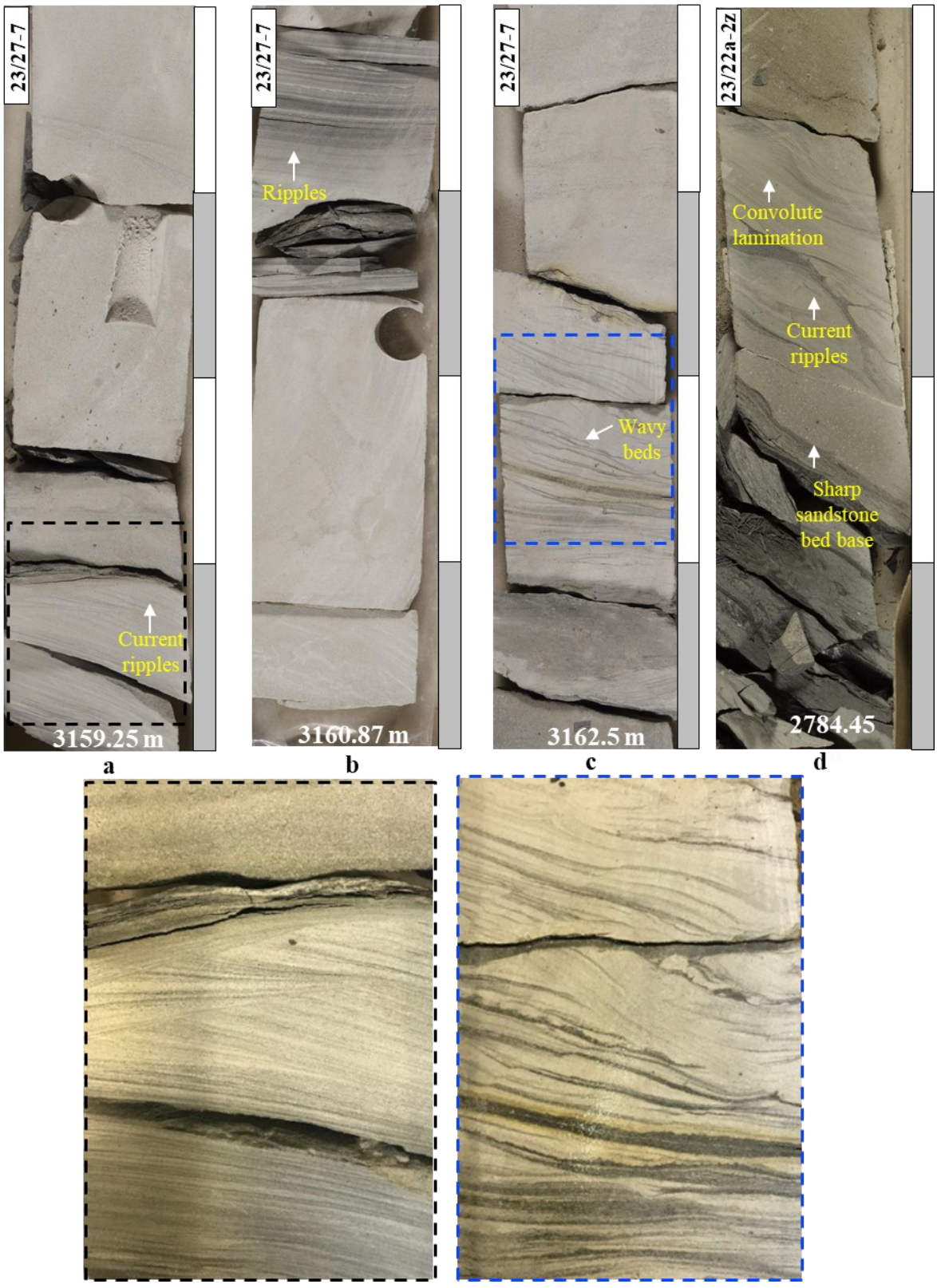
23/27-7
Current ripples
3159.25 m
a
23/27-7
Ripples
3160.87 m
b
23/27-7
Wavy beds
3162.5 m
c
23/22a-2z
Convolute lamination
Current ripples
Sharp sandstone bed base
2784.45
d

Figure 13.

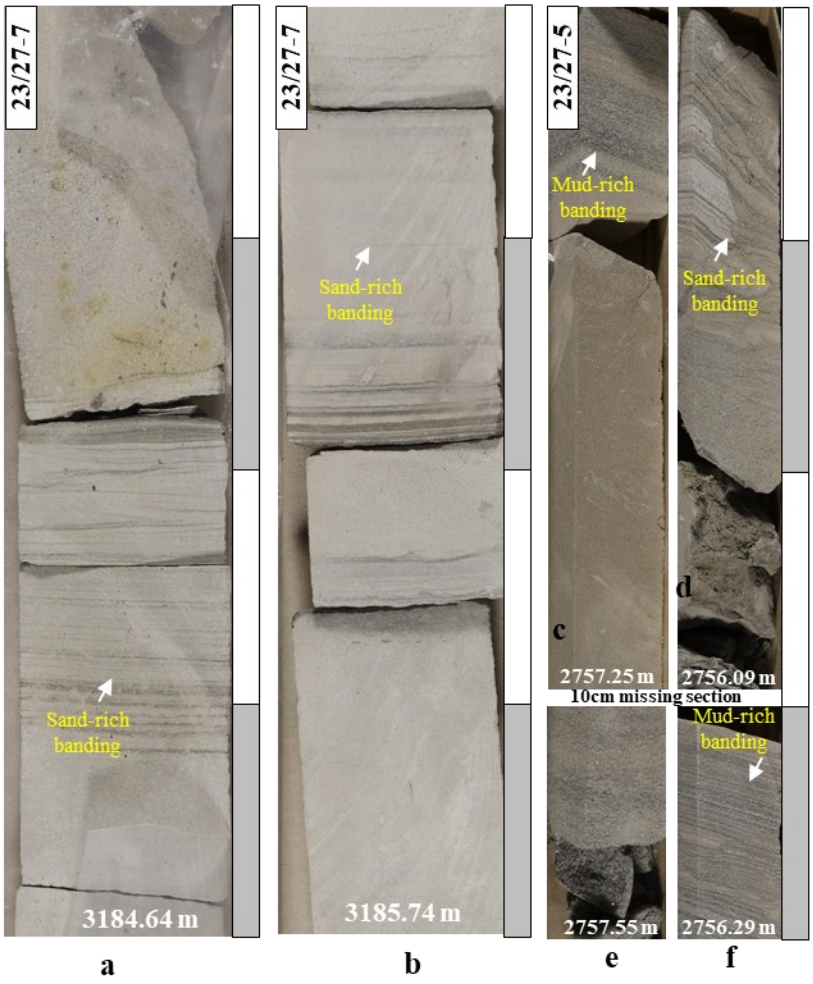
23/27-7
Sand-rich banding
3184.64 m
a
23/27-7
Sand-rich banding
3185.74 m
b
23/27-5
Mud-rich banding
c
2757.25 m
d
Sand-rich banding
2756.09 m
10cm missing section
Mud-rich banding
2757.55 m
e
2756.29 m
f

Figure 14.

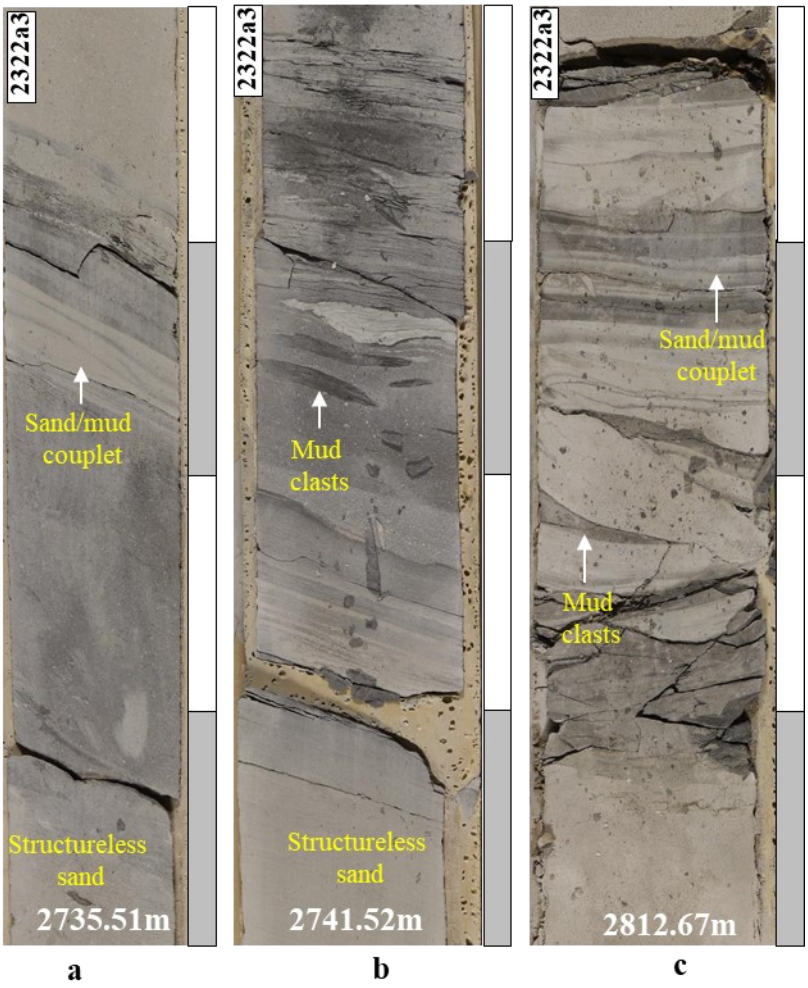
2322a3
Sand/mud couplet
Structureless sand
2735.51m
a
2322a3
Mud clasts
Structureless sand
2741.52m
b
2322a3
Sand/mud couplet
Mud clasts
2812.67m
c

Figure 15.

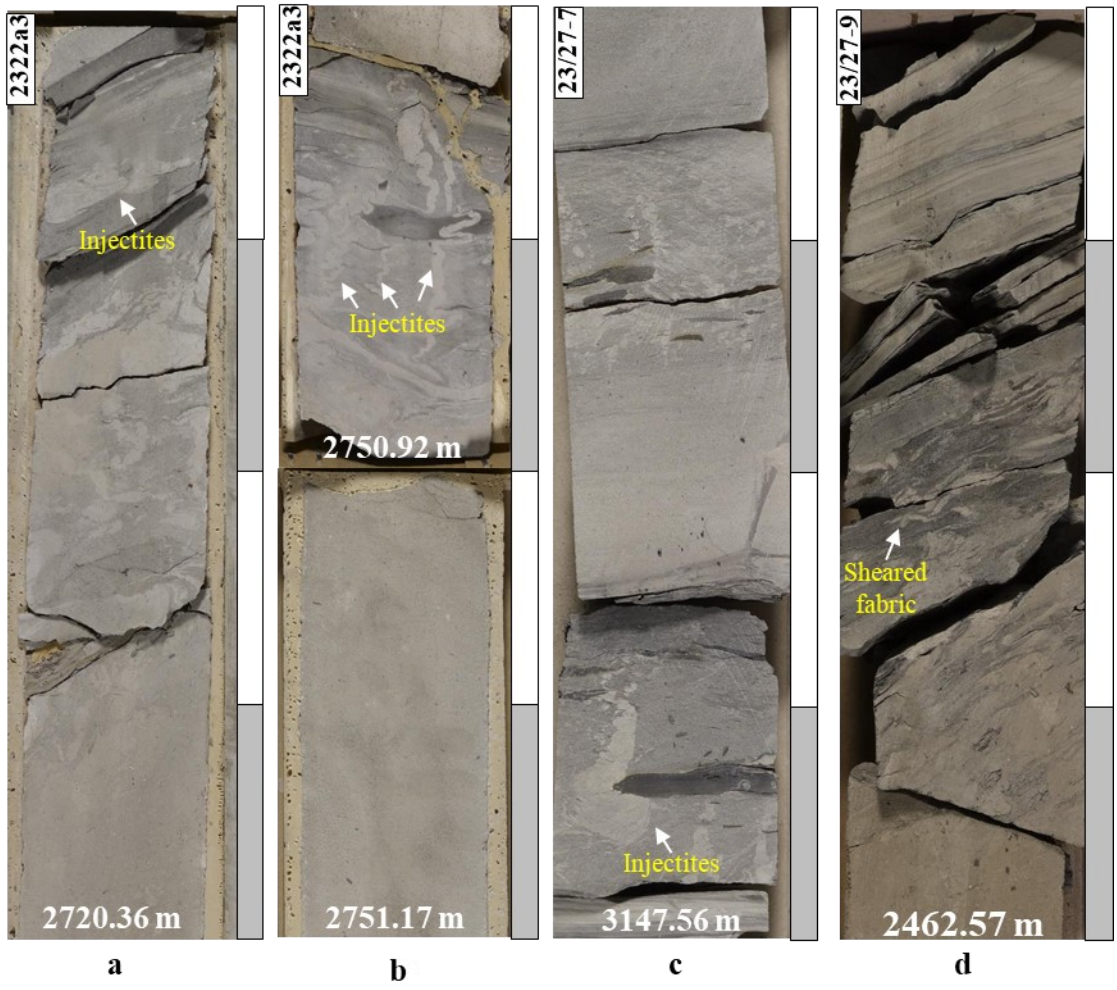
2322a3
Injectites
2720.36 m
a
2322a3
Injectites
2750.92 m
2751.17 m
b
23/27-7
Injectites
3147.56 m
c
23/27-9
Sheared
fabric
2462.57 m
d

Figure 16.

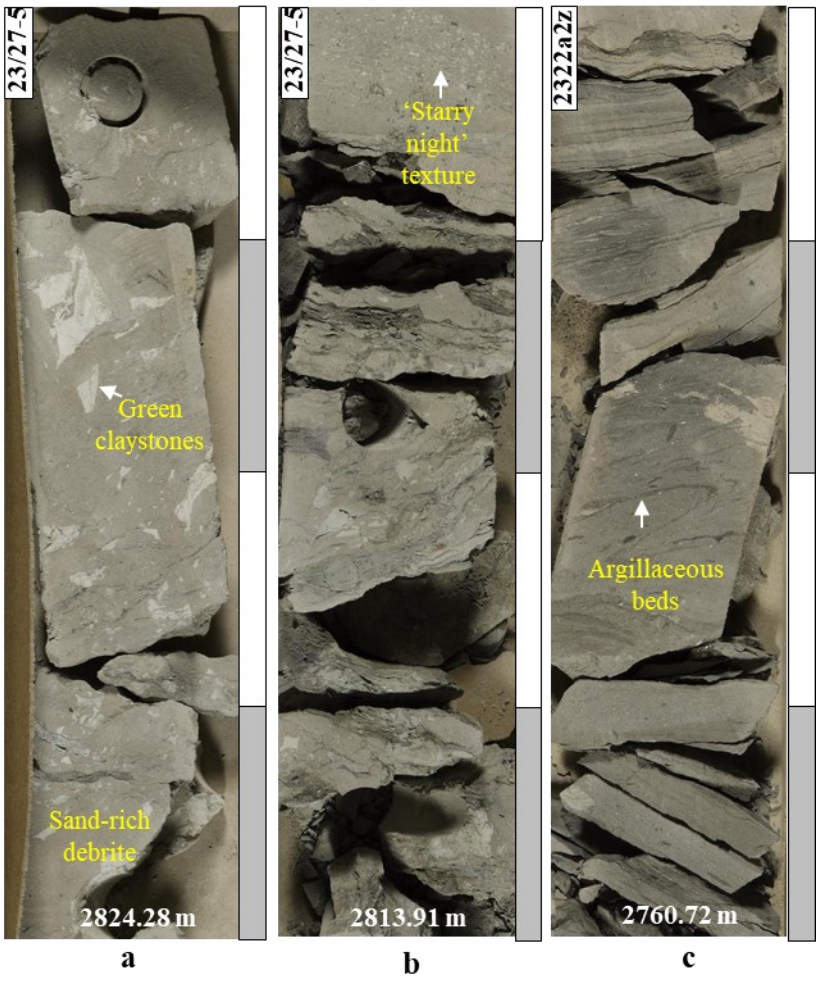
23/27-5
Green claystones
Sand-rich debrite
2824.28 m
a
23/27-5
'Starry night' texture
2813.91 m
b
2322a2z
Argillaceous beds
2760.72 m
c

Figure 17.

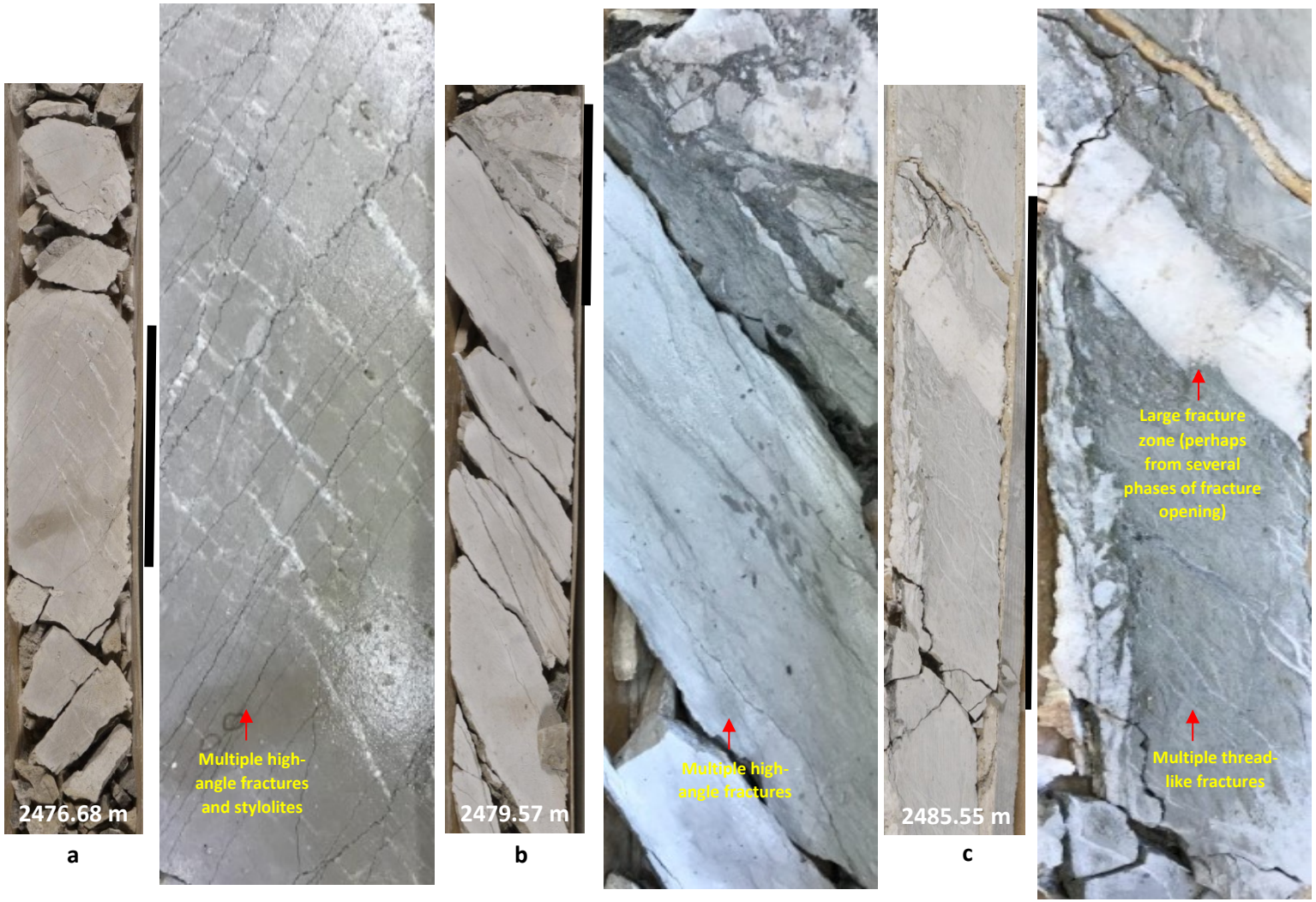
2476.68 m
a
Multiple high-angle fractures and stylolites
2479.57 m
b
Multiple high-angle fractures
2485.55 m
c
Large fracture zone (perhaps from several phases of fracture opening)
Multiple thread-like fractures

Figure 18.

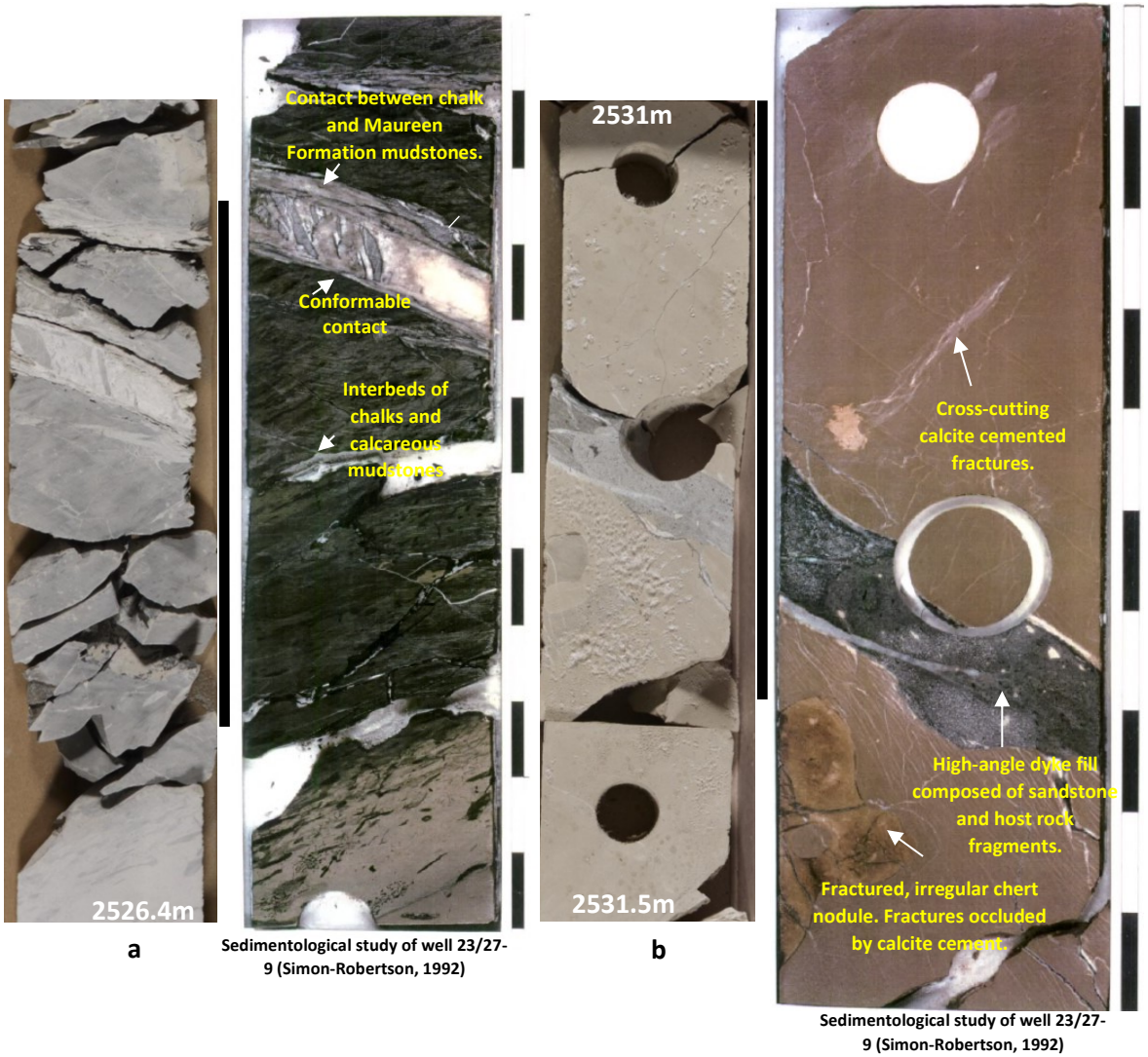

a

Sedimentological study of well 23/27-9 (Simon-Robertson, 1992)

b

Sedimentological study of well 23/27-9 (Simon-Robertson, 1992)

Figure 19.

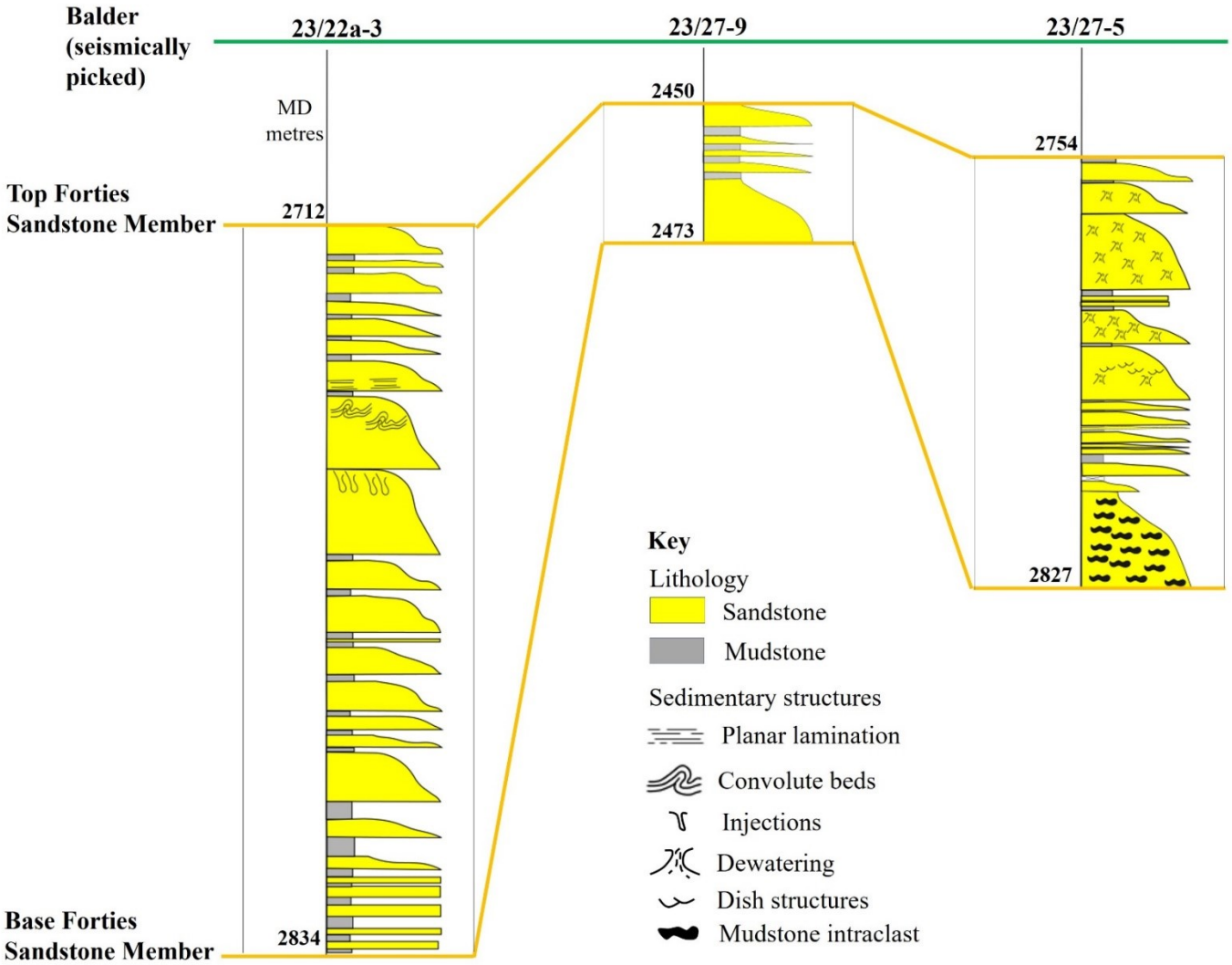
Balder
(seismically
picked)
23/22a-3
23/27-9
23/27-5
MD
metres
2450
2754
Top Forties
Sandstone Member
2712
2473
Key
Lithology
Sandstone
Mudstone
2827
Sedimentary structures
Planar lamination
Convolute beds
Injections
Dewatering
Dish structures
Mudstone intraclast
Base Forties
Sandstone Member
2834

Figure 20.

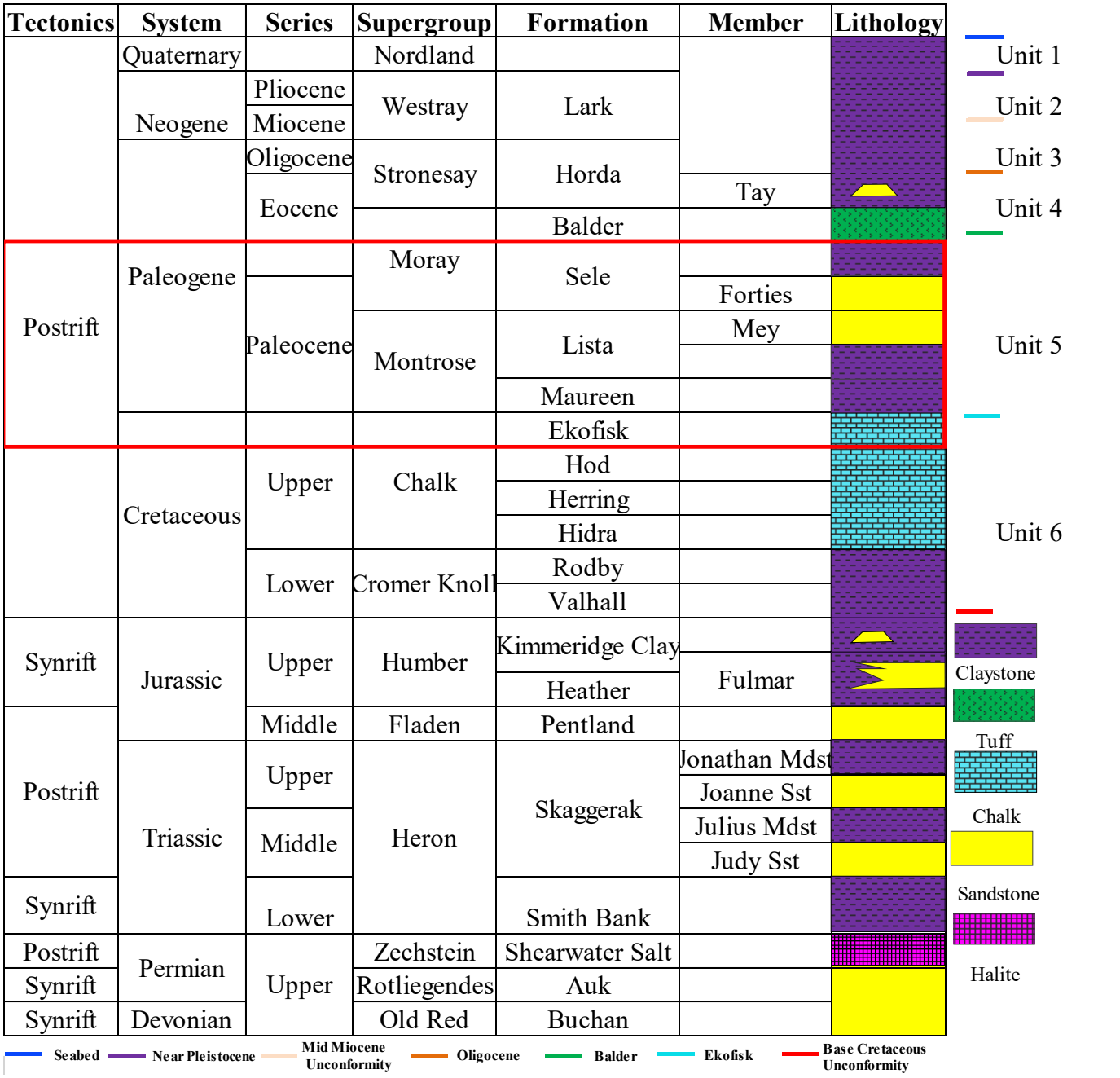
Tectonics
System
Series
Supergroup
Formation
Member
Lithology
Quaternary
Nordland
Pliocene
Neogene
Miocene
Westray
Lark
Oligocene
Stronesay
Horda
Eocene
Tay
Balder
Postrift
Paleogene
Moray
Sele
Forties
Paleocene
Montrose
Lista
Mey
Maureen
Ekofisk
Cretaceous
Upper
Chalk
Hod
Herring
Hidra
Lower
Cromer Knoll
Rodby
Valhall
Synrift
Jurassic
Humber
Kimmeridge Clay
Heather
Fulmar
Middle
Fladen
Pentland
Triassic
Skaggerak
Jonathan Mdst
Joanne Sst
Julius Mdst
Judy Sst
Heron
Smith Bank
Permian
Zechstein
Shearwater Salt
Rotliegendes
Auk
Devonian
Old Red
Buchan
Unit 1
Unit 2
Unit 3
Unit 4
Unit 5
Unit 6
Claystone
Tuff
Chalk
Sandstone
Halite
Seabed
Near Pleistocene
Mid Miocene Unconformity
Oligocene
Balder
Ekofisk
Base Cretaceous Unconformity

Table 1.

Facies Name	Description	Interpretation	Petrophysical expression
Thick-bedded sandstones (F1)	Very fine- to fine-grained sandstone with occasional coarser grains and traces of glauconite. Grains are sub-angular to sub-rounded. Sandstone occurs in 0.3->0.6 m thick beds. The beds are sharp-based and are ungraded or slightly fine-upward. They are massive at their bases (Fig. 12), sometimes with scattered pebbles or intraclasts of angular to rounded mudstone clasts. In some instances, these facies exhibit parallel stratification, followed by a zone of dewatering structures. Dewatering structures dominate the cleaner, lower part of the sandstone, and most dish structures are present in the higher, more organic-rich part. The upper part of the beds may show parallel stratification (especially in very fine-grained sands), climbing ripples, or mud-draped ripples and trough cross-beds. A layer of organic debris (0.02-0.07m thick) drapes these beds. Dewatering structures, including sandstone injections, may have destroyed all internal structures in the bed's upper part.	**High-density turbidites:** The sediments are rapidly deposited from high-density turbidity currents and might represent a preferential deposition of the sediment load due to decreased flow competence. Grains may have been buried before bedload movement, thus promoting a lack of lamination and suppressing the formation of sedimentary structures (Baas, 2011; Mulder & Alexander, 2001; Mutti & Ricci Lucchi, 1978; Stow & Johansson, 2000; Talling 2012). Alternatively, rapid mass deposition may have occurred, and open grain packing may collapse during or after the deposition of the entire bed, resulting in the escape of extra pore fluid and the formation of fluid escape structures. Both dish structures and dewatering pipes are due to the post-depositional escape of water from the sand. Dishes might be produced from a slow, horizontal flow of water controlled by semi-permeable, flat-lying barriers or depositional laminations (Collinson et al., 2019)	GR 27.80 – 66.67 API DT- 83.42 - 91.96ms/ft NPHI 0.18 - 0.27 m^3/m^3 RHOB 2.24-2.47 g/cm^3
Thin-bedded sandstones (F2)	Very fine to fine grained sandstones. Grains are sub-angular to sub-rounded. They comprise 0.03-0.1 m-thick sandstone-siltstone beds that are typically graded. The sandstone bed bases are sharp and planar to weakly erosional, and bed tops may be sharp or normally graded. The beds commonly show climbing ripple cross lamination, parallel lamination, wavy and convolute beds (Fig. 13). The sandstones may occur in thin sets interbedded with mudstones or as individual sandstone beds above high-density turbidites (i.e., thin-bedded sandstones).	**Low-density turbidites:** The sediments are deposited from low-density turbidity currents and might represent the thinner bedded turbidites associated with the thickly bedded sandstones of the main reservoir. Deposition may result from a decrease in flow velocity or flow density or interaction with a bottom current across the path of the turbidity current (Stow & Omoniyi, 2018). They typically represent the classic Bouma Tc/d/e divisions ((Lowe and Guy 2000; Barker et al., 2008). The parallel laminations of the 'B' division record the upper flow regime plane bed, whereas the 'C' division records ripple migrating under a weaker current in the lower flow regime. The D and E divisions result from direct deposition from suspension. Thin-bedded sandstones are distributed extensively in both marine and lacustrine settings.	GR – 42.66-47.77 API DT – 79.62 – 90.55 ms/ft NPHI – 0.14 – 0.24 m^3/m^3 RHOB- 2.29 – 2.38 g/cm^3

Facies Name	Description	Interpretation	Petrophysical expression
Banded sandstones (F3)	Very fine- to medium-grained sandstone. Grains are sub-angular to sub-rounded. Sandstone bed (0.05 – 0.15m thick) comprises alternating light and dark, centimeter-scale, parallel to sub-parallel laminations or bands. The dark bands are mud-rich (matrix and clasts), matrix-supported, and poorly sorted. The light bands (grain supported and better sorted) comprise planar laminated clean sandstone (Fig. 14). I observe meso- (0.01-0.1m) to macro-banding (0.1-0.5 m) within this unit. They overlie a structureless basal sandstone (F1) and may be capped by clean, parallel-laminated sandstone or ripple cross-lamination sandstone. Bands generally have sharp upper and lower contacts, with cleaner bands loading into dirty bands.	**Transitional flows:** The sediments are deposited from transitional flows interchangeable between turbidity currents and laminar (cohesive) flows. Banding signifies hydrodynamically distinct sand and mud grain sizes deposited under similar flow conditions in alternating layers. Banding can originate from bedform development under mud-rich transitional flows (Baas et al., 2011), from episodic, near-bed turbulence damping (Lowe and Guy, 2000), or from longitudinal flow transformation that suppresses turbulence and generates a cohesive laminar plug (Haughton et al., 2009). Microbanding (up to 15 cm) from the core analysis has been reported in the Paleogene Forties Fan and represents deposition in a fan-fringe setting (Haughton et al., 2009). Banded sandstones occur in proximal settings, e.g., base-of-slope channel-mouth settings of the Geelbek River, South Africa (Hofstra et al. 2015, Stevenson et al. 2020), Magnus oilfield (Ravnas et al. 2000, Stevenson et al. 2020).	GR – 34.99-60.66 API DT – 85.15-99.58 ms/ft NPHI - 0.20-0.27 m^3/m^3 RHOB- 2.32-2.34 g/cm^3
Hybrid beds (F4)	A combination of high-density turbidite (F1) at the lower part of the bed and an upper debrite. Five internal divisions are possible. Typically the lower main part of the bed is dominated by a fine- to medium-grained banded sandstone or structureless sandstone (F1) with crude consolidation lamination. This is overlain by a crude banding defined by slightly pale (cleaner) band tops with floating mud clasts and deformed dewatering structures. A subsequent layer contains mud clasts (m), a uniform dark muddy sandstone with a carbonaceous flake towards the top. The event bed is capped by a parallel to ripple laminated very fine-grained sandstone in which clay aggregates are effectively segregated creating darker laminae and foresets (Fig. 15). Bed bases are generally sharp and planar, with loading or erosional sole structures. The transition from clean to argillaceous sandstone is gradational or relatively flat. Hybrid event beds are generally dcm to m thick, extending down to a few cm and up to >10 m thick. The muddy upper part shows significant vertical segregation of components such as mud clasts, outsized sand grains, and carbonaceous matter.	**Hybrid event beds**: The sediments are emplaced by a combination of fluidal and plastic flow recording, switching between turbulent, transitional, and laminar behavior. Similar and related beds have been encountered in a range of other turbidite systems (e.g., Sylvester and Lowe, 2004; Talling et al. 2004) and in outcrop studies. Hybrid beds are commonly found in the lateral (valley-transmitting and filling flows) and distal (valley-incising flows) part of deep-water fans and basin plain sheet systems (Haughton et al 2009), suggesting episodes when flows became choked with mud clasts, alternating with times when flows remained largely turbulent. Hybrid event beds are documented in the Forties fan system (Haughton et al. 2009). Mud clasts within the upper argillaceous part of many event beds suggest the onset of laminar or weakly turbulent flow conditions and can be eroded from underlying siltstone. The capping beds may result from low-density turbidites and mud suspension fall-out. Deformed dewatering structures suggest shearing by an overriding flow.	GR-28.21-49.85 API DT-62.52-92.01 ms/ft NPHI-0.055-0.21 m^3/m^3 RHOB-2.33-2.62 g/cm^3

Facies Name	Description	Interpretation	Petrophysical expression
Slurry beds (F5)	This facies consists of fine-grained sandstone, siltstones, and mud-rich sandstones (Fig. 16). Individual beds are 0.25-0.7 m-thick and exhibit folded and sheared textures, injected mudstone intervals, ball-and-pillow structures, soft-sediment deformation structures or disturbed strata (steeply dipping, folded, overturned, or fractured by extensional microfaults). Water-escape structures may be present including vertical to sub-vertical pipe- and sheet-like fluid escape structures.	**Slurry flows** are transported by highly fluid, silty debris flows. The beds are rapidly deposited from concentrated flows, due to a combination of increased cohesion and intergranular friction. Contorted strata may result from gravity-induced sliding during which rotational slumping and internal deformation occurs (Lowe and Guy 2003). They are sourced from mud-rich substrate.	GR - 21.71 - 80 API DT – 63.71-99.87 ms/ft NPHI – 0.05-0.29 m^3/m^3 RHOB- 2.33-2.57 g/cm^3
Debrites (F6)	These facies range in spectrum from 0.1->1m thick mud-rich matrix-supported, clast-rich fine-medium grained muddy sandstones to 0.1->1m-thick siltstone to fine-sandstone rich mudstones with starry-night texture. Clasts within the 'muddy sandstones' are often sub-rounded to angular, with sheared and squeezed texture. Small clasts within the 'sandy mudstones' are mostly dark mudstones, subrounded to angular or sheared and aligned parallel to bedding. The beds are poorly sorted and show little or no internal organization. The units have flat, sharp and irregular upper contacts. (Fig. 17).	**Debris flow:** The sediments are emplaced by en-masse freezing of laminar or weakly turbulent cohesive flows (Haughton et al. 2009). They are commonly sourced from unstable slopes, upper-mid slope and base-of-slope. The starry-night texture is made up of predominantly granule to pebble-grade clasts of quartz, mudstones and carbonaceous material, supported within the mudstone matrix.	GR - 33.55 – 54.31 API DT – 71.1– 122.9 ms/ft NPHI – 0.15-0.26 m^3/m^3 RHOB -2.41 - 2.53 g/cm^3

Facies Name	Description	Interpretation	Petrophysical expression
Mudstone (F7)	Massive or homogeneous mudstones and siltstone beds. They can be up to 4 m in thickness. No sedimentary structure or bioturbation or fragments was observed. They have sharp upper and lower contacts. Green claystones are common in the 23/27-5 well and are fissile to sub-fissile, non-calcareous, slightly mottled and waxy in composition.	**Mudstones:** these sediments may be deposited by a diversity of processes including low-concentration thick turbidity currents, thin turbid layer flows, bottom (contour currents), hemipelagic and pelagic deposition (Stow and Shanmugam 1980). They occur in association with other sediment gravity flow deposit and represent the fine-grained, tail fraction of a turbidity current. They are common in slope and basin floor environments. They may represent a period of inactivity due to channel switching or overall fan abandonment.	GR 70 – 87 API NPHI 0.27-0.35 m^3/m^3 RHOB 2.28-2.53 g/cm^3
Chalk (F8)	Moderately hard to hard, blocky to angular, chalky, mudstone texture. There is conformable contact between overlying Maureen Formation mudstones and the chalk (Fig. 19a). These facies contain dyke fills of subarkosic sandstones and fractured chert nodules (Fig. 19b) formed at high angle to bedding. It also comprises numerous intensely fractured interval with multiple thread-like fractures and large fracture sets (Figs. 18a,b,c). Principal fracture sets are aligned parallel, subparallel, high-angle and normal to bedding. Multiple fracture reactivations are present and are partially or wholly filled by calcite. Coarse crystalline calcite microveins, stylolites, subvertical fracture with calcite and mudstone infill, occasional vugs are common (Fig. 18a). These facies are extensively bioturbated in places, likely destroying any primary physical sedimentary structures. Bedding parallel microstylolite swarm has concentrated terrigeneous mud, pyrite, and bioclastic debris.	Deposited in outer shelf to basinal environment as a pelagic 'rain' of coccolithophorid algae and planktonic foraminifera resulting in autochthonous chalks (Simon-Robertson, 1992). Although not immediately evident from the cores reviewed in this study, brecciation and chaotic units in some reported fields, e.g Kyle Field, Central North Sea, (Davison et al., 2000) provides some evidence for re-sedimentation. Sand dykes may have been derived from passive infiltration or injection from overlying Maureen Formation. The large fracture sets may have resulted from several phases of fracture opening with wall-rock slivers separating each 'crack and heal' event. Microstylolite swarm/solution seam may indicate pressure solution that has preferentially occurred at a primary bedding contact (Simon-Robertson, 1992, Petrographic study of well 23/27-9). Bioturbated intervals contains Chondrites, Zoophycus and Thalassinoides burrows and reflects abundance of matrix microporosity (Simon-Robertson, 1992).	GR 7.3 – 21 API NPHI 0.07-0.21 m^3/m^3 RHOB 2.33-2.61 g/cm^3

Table 2